

# Identification of Low-Level Point Radioactive Sources Using a Sensor Network

JREN-CHIT CHIN

Purdue University

NAGESWARA S. V. RAO

Oak Ridge National Laboratory

DAVID K. Y. YAU

Purdue University

MALLIKARJUN SHANKAR

Oak Ridge National Laboratory

YONG YANG and JENNIFER C. HOU

University of Illinois at Urbana-Champaign

and

SRINIVASAGOPALAN SRIVATHSAN and SITHARAMA IYENGAR

Louisiana State University

Identification of a low-level point radioactive source amidst background radiation is achieved by a network of radiation sensors using a two-step approach. Based on measurements from three or more sensors, a geometric difference triangulation method or an  $N$ -sensor localization method is used to estimate the location and strength of the source. Then a sequential probability ratio test based on current measurements and estimated parameters is employed to finally decide: (1) the presence of a source with the estimated parameters, or (2) the absence of the source, or (3) the

---

A preliminary version of this article was presented at 2008 ACM/IEEE International Conference on Information Processing in Sensor Networks (IPSN), and appears in the conference proceedings [Rao et al. 2008].

Research was supported in part by the U.S. Department of Energy under SensorNet grant no. AC05-OOOR22725 and Mathematics of Complex, Distributed, Interconnected Systems program, Office of Advanced Computing Research, and in part by the U.S. National Science Foundation under grant no. CNS-0964086; work was performed at Purdue University and Oak Ridge National Laboratory managed by UT-Battelle, LLC.

Author's address: J.-C. Chin: email: jechin@cs.purdue.edu.

©2010 Association for Computing Machinery. ACM acknowledges that this contribution was authored or co-authored by a contractor or affiliate of the U.S. Government. As such, the Government retains a nonexclusive, royalty-free right to publish or reproduce this article, or to allow others to do so, for Government purposes only.

Permission to make digital or hard copies of part or all of this work for personal or classroom use is granted without fee provided that copies are not made or distributed for profit or commercial advantage and that copies show this notice on the first page or initial screen of a display along with the full citation. Copyrights for components of this work owned by others than ACM must be honored. Abstracting with credit is permitted. To copy otherwise, to republish, to post on servers, to redistribute to lists, or to use any component of this work in other works requires prior specific permission and/or a fee. Permissions may be requested from Publications Dept., ACM, Inc., 2 Penn Plaza, Suite 701, New York, NY 10121-0701 USA, fax +1 (212) 869-0481, or permissions@acm.org. © 2010 ACM 1550-4859/2010/09-ART21 \$10.00

DOI 10.1145/1807048.1807050 <http://doi.acm.org/10.1145/1807048.1807050>

insufficiency of measurements to make a decision. This method achieves specified levels of false alarm and missed detection probabilities, while ensuring a close-to-minimal number of measurements for reaching a decision. This method minimizes the ghost-source problem of current estimation methods, and achieves a lower false alarm rate compared with current detection methods. This method is tested and demonstrated using: (1) simulations, and (2) a test-bed that utilizes the scaling properties of point radioactive sources to emulate high intensity ones that cannot be easily and safely handled in laboratory experiments.

Categories and Subject Descriptors: C.2.1 [**Network Architecture and Design**]: Source Localization

General Terms: Algorithms, Design, Experimentation, Performance

Additional Key Words and Phrases: Point radioactive source, detection and localization, sequential probability ratio test

**ACM Reference Format:**

Chin, J.-C., Rao, N. S. V., Yau, D. K. Y., Shankar, M., Yang, Y., Hou, J. C., Srivathsan, S., and Iyengar, S. 2010. Identification of low-level point radioactive sources using a sensor network. ACM Trans. Sensor. Netw. 7, 3, Article 21 (September 2010), 35 pages.

DOI = 10.1145/1807048.1807050 <http://doi.acm.org/10.1145/1807048.1807050>

---

## 1. INTRODUCTION

There has been an increasing interest in the identification of *low-level* radioactive sources as a part of the defense strategy against dirty bomb scenarios. The ability to identify the signatures of such sources will enable their detection before they are set off, in particular, while the sources are being transported or stored. Or, in another scenario, we will be able to detect radiation traces and estimate their extent in seemingly conventional explosions, so that first responders can be forewarned and suitably protected against the low-level yet highly hazardous radiation. Typically, in both of these scenarios, the radiation levels may be low enough to appear as “normal” variations of the background radiation. The detection problem is particularly acute since the radiation measurements follow the Poisson process, whose variance is equal to the radiation level itself. While long-term averages of low-level sources do result in elevated levels which eventually can be detected, our focus is on identifying the sources quickly to ensure fast response. In general, the area of detecting various radioactive sources using individual sensors has been well established in terms of both detection devices and detection methods [Knoll 2000; Nelson et al. 2007], most of which are dedicated to single or co-located sensor systems. Recent advances in sensor network technologies, however, have opened up the potential for improved detection, as well as the estimation of source parameters, by utilizing measurements from multiple, geographically dispersed sensors; see, for example, [Brennan et al. 2004; Gunatilaka et al. 2007; Mielke et al. 2005; Nemzek et al. 2004; Stephens and Peurrung 2004; Sundaresan et al. 2007] for this line of work.

Compared with the identification of high intensity radioactive sources, detection and localization of low-level sources is difficult due to two major issues.

- (A) *Varied Background Radiation.* The background radiation depends on both local natural and man-made sources and global sources such as cosmic rays, and hence it may vary significantly from one deployment region to

another. If not carefully interpreted, such measurements lead to “ghost” sources (false alarms) that may cause unnecessary panic.

- (B) *Probabilistic Radiation Measurements.* The radioactive sources generate inherently probabilistic measurements; typically, gamma radiation from point sources follows the Poisson distribution [Knoll 2000; Mihalas and Mihalas 2000].

The combined effect of these two factors makes it hard to derive *a priori* thresholds needed by traditional detection methods. Furthermore, the estimation of source location parameters cannot be directly solved by the triangulation methods developed for deterministic measurements. On the other hand, the estimation can be made more effective when a network of sensors is employed, provided that a number of remaining estimation problems can be solved. In this paper, we address Issue (A) above by in-situ estimation of background radiation during initial network deployment. We address Issue (B) above using a combined geometric localization method and the sequential probability ratio test (SPRT).

Probability ratio tests are typically employed in the *detection* problems to derive thresholds to achieve specified levels of false alarm rates and missed detection rates, in both centralized [Trees 1968] and distributed detection systems [Varshney 1997]. Such an approach is described for the detection of radioactive sources using single sensors in Fehlau [1993], Jarman et al. [2004], and Nelson et al. [2007] (to name a few examples) and using copula methods in sensor networks [Sundaresan et al. 2007]. The estimation of the location and strength of point radioactive sources typically requires at least three sensors and is solved using the least square methods in Howse et al. [2001], Gunatilaka et al. [2007], and Morelande et al. [2007]. Typically, the *parameter estimation* methods implicitly assume that the measurements are due to a real source, and not just the background, often by utilizing a preceding detection step. For low-level sources, however, it is not as easy to discriminate between source and background measurements, and existing methods often return results corresponding to “ghost” sources.

In this article, we show that the detection and parameter estimation steps can reinforce each other, in a two-step decision procedure for low-level radioactive sources. We present a method for the *identification*—which subsumes the detection and parameter estimation problems—of a point radioactive source using a network of three sensors that provide radiation counts. In the first step, we utilize a localization method to estimate the location of a real or ghost source, from which we also estimate the source strength. Then, using the estimated source parameters, we utilize SPRT to declare: (1) the presence of a source with the estimated parameters, (2) the absence of the source, or (3) the insufficiency of the collected measurements to make a decision. The 3-sensor localization method is derived by adapting the recently developed geometric difference-triangulation method [Rao et al. 2007] to our problem, which does not have the numerical vulnerabilities of least squares or linear methods. The source strength is estimated using a linear combination of the estimates from individual sensors. The  $N$ -sensor localization method is based on the iterative

pruning (ITP) algorithm in Chin et al. [2008]. ITP increases the robustness of the estimation in the face of noise and errors in the measurement process. The detection test utilizes the estimated background radiation of the given deployment region and the estimated source parameters, to formulate SPRT based on the Poisson point source model. Ghost sources, if estimated in the first step, will be rejected by the SPRT to ensure a specified false alarm rate, since they do not lead to statistically consistent measurements. On the other hand, the estimated parameters enable us to formulate a more specific SPRT compared with detecting a general increase in the radiation level, which in turn yields a decision with the least expected number of measurements. Our approach is in contrast to conventional approaches in which detection precedes identification as in several tracking applications [Blackman and Popoli 1999; Bar-Shalom and Li 1995].

Evaluating identification methods for radioactive sources poses pragmatic challenges of experimentation, since it is potentially hazardous and too expensive to deploy radioactive sources of all but minimal strengths. We exploit the simple product form of the radiation model to develop a scaled-down workbench that emulates higher-intensity sources and larger-scale deployments. In particular, we map the workbench of a few feet in dimension to emulate deployments of several hundred meters, and demonstrate the effectiveness of our method using real but safe low-level radioactive sources.

The balance of the article is organized as follows. In Section 2, we briefly review related work on the detection and estimation of radiation sources, with an emphasis on sensor network solutions. We formulate the identification problem in Section 3. We describe our solution to the source parameter estimation problem in Section 4 and the detection problem in Section 5. We combine the estimation and detection results to develop our identification method in Section 6, for both cases of 3 sensors and  $N$  sensors. We present our simulation results in Sections 4, 5, and 6, and test-bed and emulation results in Section 7.

## 2. RELATED WORK

The detection and identification problems have been studied extensively over the past several decades in the areas of signal detection [Poor 1998; Macmillan and Macmillan 2004; Wickens 2002], classification [Devroye et al. 1997; Duda et al. 2001], estimation [Bar-Shalom and Li 2001; Kushner and Yin 2003], identification [Ljung 1998] and tracking [Blackman and Popoli 1999], under various formulations. Traditionally, the presence of a source is confirmed based on measurements using a detection or classification rule first. Then, the measurements are used to estimate the parameters using an underlying linear or nonlinear model with random noise components. For example, one of the most studied formulations, the Kalman filter, assumes a linear process model with additive independent Gaussian noise. Our formulation requires a combination of these two approaches since it does not presuppose the presence of a source and yet requires its parameter estimates if it is indeed present. Furthermore, the underlying Poisson measurements are inherently random with a high variance, which are characteristically different from the Gaussian measurements.

These differences are reflected in our solution which utilizes the source parameter estimates to sharpen the decision performance. Furthermore, compared with these general estimation and identification methods, our source parameter estimates more closely exploit the quadratic decay behavior of the source strength with respect to distance.

Within the discipline of radiation detection, the detection and estimation of radioactive sources of various kinds have been well studied, particularly using single sensors [Knoll 2000; Archer et al. 2006]. The detection of radioactive sources amidst background radiation has been studied using SPRT for various scenarios such as long-term and portal monitoring [Fehlau 1993; Jarman et al. 2004; Nelson et al. 2007]. The existing work using SPRT does not address the source localization problem.

The use of a network of sensors for detecting and tracking radioactive sources has been more recently proposed. For the detection of radioactive sources, a linear arrangement of detectors has been considered in Nemzek et al. [2004], Brennan et al. [2004], and Mielke et al. [2005], and an analysis of sensor network solutions has been carried out for a source moving in a linear path [Stephens and Peurrung 2004]. The detection of a point radioactive source using a sensor network is addressed in Sundaresan et al. [2007], wherein sensor measurements are combined using a copula function that captures the sensor correlations.

Typically, a detection method is used to first assert the presence of a radiation source, and *then*, measurements from multiple sensors are used to estimate the parameters of the source. The problem of localizing a point radioactive source has been addressed in Gunatilaka et al. [2007], Morelande et al. [2007], and Anderson et al. [2006]. Recursive and moving horizon non-linear least square methods have been proposed to track radioactive sources in Howse et al. [2001]. Overall, the existing estimation methods assume that the measurements correspond to a real source (i.e., the source does exist), whereas the detection methods are most effective when the source parameters are accurately known. Our focus in this article is to jointly address the detection and estimation problems by closely coupling the two decisions.

Detection, localization, and tracking of other types of signal sources have also been studied in the past, for instance, localization of a chemical plume by using data taken periodically from a network of chemical sensors [Gunatilaka et al. 2008]. Their algorithm assumes that the chemical is being released on the ground continuously. It utilizes a sequential Bayesian framework, and Monte-carlo integration to compute the most likely position of the chemical plume. Ding and Cheng [2009] use multi-modal sensor data to localize and track signal sources by modeling the sources with a Gaussian mixture model and then using Bayesian Information Criterion, a model selection algorithm, to estimate the number of sources. Then, an expectation maximization algorithm and mean-shift algorithm are used to localize and track the sources. All the above techniques rely on measured signal strengths to infer the location of the signal source. The localization task in wireless network is accomplished using Time Difference-of-Arrival (TDOA) methods [Savvides et al. 2001; Cheng et al. 2004; Thaeler et al. 2005] that measure differences in signal arrival times at different sensors, and Angle-of-Arrival (AoA) methods [Niculescu and Nath

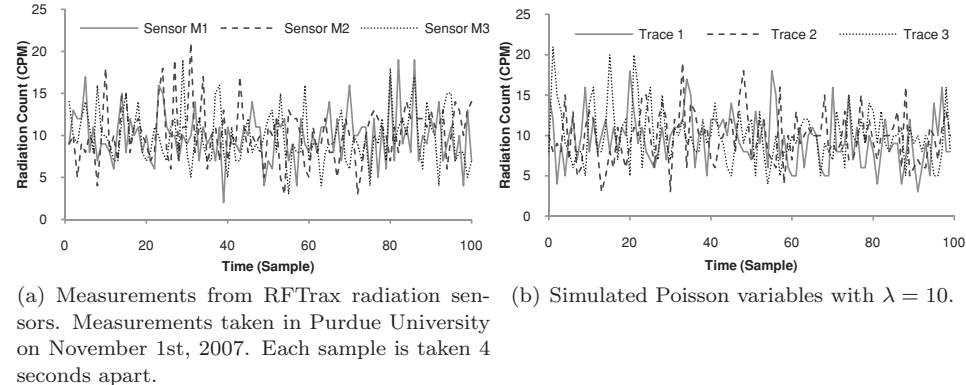


Fig. 1. Actual and simulated background radiation measurements.

2003] that measure the signal incident angles at different sensors. Unlike the signal strength-based methods, the TDOA methods require accurate time synchronization among the sensors, whereas AoA requires directional antenna for its operation.

### 3. PROBLEM FORMULATION

We consider the identification of a point radioactive source  $S$  of unknown strength  $A_u$  expressed per unit time called the *source rate*, and located at an unknown location  $(x_u, y_u)$ . The source gives rise to a radiation intensity of  $I(x, y) = A_u/r^2$  at any point  $(x, y)$ , where  $r = d((x_u, y_u), (x, y)) = \sqrt{(x_u - x)^2 + (y_u - y)^2}$ . Let  $m_{i,1}, m_{i,2}, \dots, m_{i,n}$  be a sequence of radiation counts, each measured per unit time, at the sensor  $M_i$  at known location  $(x_i, y_i)$ , for  $i = 1, 2, 3, \dots$ . The radiation count due to the source observed at  $M_i$  per unit time is a Poisson random variable with parameter  $\lambda = I(x_i, y_i)$ , not accounting for the background radiation [Knoll 2000; Mihalas and Mihalas 2000].

Let  $B(x, y)$  denote the background radiation strength at  $(x, y)$  expressed in unit time, called the *background rate*. The radiation count measurement (due to the background radiation) at a sensor  $i$  located at  $(x_i, y_i)$  is given by the Poisson random variable with parameter  $B(x_i, y_i)$ . The assumption of Poisson distribution for the background measurements may not always be accurate, since the background radiation may be a complex combination of various sources. However, for our purpose, modeling the background measurements using the Poisson distribution is accurate enough. Figure 1(b) shows the similarity between actual sensor measurements and Poisson-generated random numbers. We utilize this assumption in our main derivation and later account for possible deviations. On the other hand, measurements of  $I(x_i, y_i)$ , being from a single point source, are more accurately characterized by the Poisson distribution. In either case, the measurements are statistically independent across the temporal dimension, and exhibit significant variations as shown in Figure 1(a).

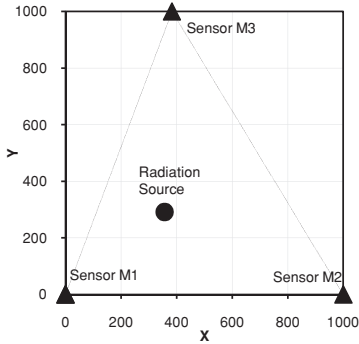


Fig. 2. An example of a region monitored by three sensors forming an acute triangle.

The *detection problem* is concerned with inferring the presence of a source, whereas the *estimation problem* is concerned with estimating the location (i.e., the localization problem) and the strength of the source, if present. The estimates of  $(x_u, y_u)$  and  $A_u$  are denoted by  $(\hat{x}_u, \hat{y}_u)$  and  $\hat{A}_u$ , respectively. We characterize the solution of the detection problem by the *false alarm probability*  $P_{1,0}$ , corresponding to the probability of declaring the presence of a source when none exists, and the *missed detection probability*  $P_{0,1}$ , corresponding to the probability of declaring the presence of only the background radiation when a source is present in the monitoring region. In addition, we characterize the timeliness of the solution method by the *detection time* which is the size of the time window or the number of measurements needed to declare the presence or absence of a radioactive source.

#### 4. SOURCE PARAMETER ESTIMATION

##### 4.1 The 3-Sensor Case

In this section, we solve the source parameter estimation using 3 sensors. We first present a method to estimate  $(\hat{x}_u, \hat{y}_u)$  using an extension of the geometric triangulation method in Rao et al. [2007]. We then describe a linear fuser to estimate the source strength  $A_u$ . We consider a monitoring area contained within the acute triangle formed by  $M_1, M_2, M_3$  (as shown in Figure 2 for an example) to simplify the presentation of the localization method; the triangle property is not needed in practice, as the presented method can be shown to work for general geometries [Rao et al. 2007; Xu et al. 2010]. We are given three sequences of measurements, from  $M_i$  for  $i = 1, 2, 3$ , collected within the same time window. These measurements are collected from the sensors and sent to a centralized server for estimating the source parameters.

**4.1.1 Location Estimation.** The location of the radiation source can be estimated by adapting the Difference of Time-of-Arrival (DTOA) algorithm to ln-space as described in the following. Let  $m_{i,1}, m_{i,2}, \dots, m_{i,n_i}$  denote a sequence of  $n_i$  measurements collected by the sensor  $M_i$  within a given time window. Using the measurements, we compute the mean of measurements at each

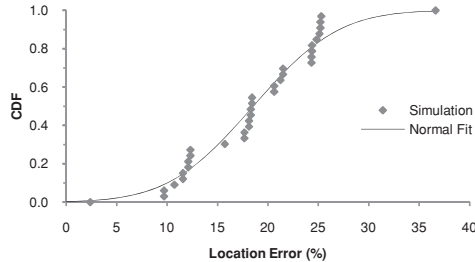


Fig. 3. Errors of location estimation method for 50 simulation runs. The curve denotes the best fit to normal distribution.

sensor given by  $\bar{m}_i = \frac{1}{n_i} \sum_{j=1}^{n_i} m_{i,j}$  for  $i = 1, 2, 3$ . The mean is an unbiased estimate of  $A_u/r_i^2$  for  $r_i = \sqrt{(x_u - x_i)^2 + (y_u - y_i)^2}$ . In terms of expectations, we have  $\frac{1}{2} \ln(E[\bar{m}_i]/E[\bar{m}_k]) = \ln r_i - \ln r_k$ , which is the difference in distances of the sensors from the source in ln-space. Let  $\delta_{i,k} = \frac{1}{2} \ln(\bar{m}_i/\bar{m}_k)$ , such that  $\delta_{i,k} = \ln r_i - \ln r_k$  is valid on average. Let  $L_{i,k}$  denote the set of all points  $(x_u, y_u)$  on a plane such that  $\ln r_i - \ln r_k = \delta_{i,k}$ . Our localization method is based on binary search on  $L_{1,2}$  using  $\delta_{1,3}$  as an objective function to locate a point  $(\hat{x}_u, \hat{y}_u)$ , such that  $|x_u - \hat{x}_u| \leq \epsilon$  and  $|y_u - \hat{y}_u| \leq \epsilon$ . The implementation details of the search algorithm can be found in Xu et al. [2010].

We now present simulation results to illustrate the performance of the above method. The simulation programs are implemented in C using random number generators from Numerical Recipes [Press et al. 1992] and executed on a Redhat Linux workstation with a 2.8 GHz Intel processor. In simulations, the position of sensor  $M_1$  and  $M_2$  are set at (0 m, 0 m) and (1000 m, 0 m). For  $M_3$ , the x-coordinate is randomly chosen from [1, 1000] m while the y-coordinate is fixed at 1000 m. A radiation source of strength<sup>1</sup>  $A_u = 10^6$  counts-per-minute (CPM) is randomly placed in the  $1000 \times 1000$  m<sup>2</sup> surveillance area. The background radiation is  $B = 10$  CPM. The simulation results are shown in Figure 3. The average error is 20.07% for 1000 randomly located sources but the errors have a high variance due to the Poisson measurements. Some example source locations and their estimators are shown in Figure 5, wherein a line segment joins the actual location of the source (shown as a filled circle) with its estimator (shown as a nonfilled circle).

To illustrate the behavior of the location estimation without a radiation source, we repeat the experiment with background radiation only, where  $B = 10$  and 100 CPM at the sensors. As shown in Figure 6, the ghost sources have been identified approximately near the centroid of the triangle formed by the sensors when the measurements are repeated. In the next section, we outline a method that utilizes the estimated source parameters in SPRT to rule out such ghost sources.

<sup>1</sup>The source strengths in the range  $[10^5, 10^6]$  counts-per-minute (CPM) are still low-level, despite their apparently large absolute magnitudes, since they generate only small increases (less than 20%) in the measurements over a 1000m  $\times$  1000m monitoring area as shown in Figure 4, due to the quadratic decay of the intensity with respect to distance.

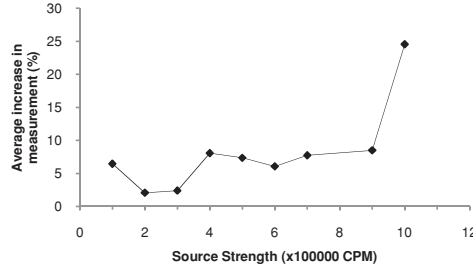


Fig. 4. Percentage increase in radiation level over the background level due to sources with  $A_u = 2 \times 10^5, 5 \times 10^5, 6 \times 10^5, 7 \times 10^5, 10 \times 10^5$  CPM. Despite the large absolute source strength magnitudes in CPM, the radiation source of  $A_u = [10^5, 10^6]$  CPM generates less than 20% increment over the background radiation count.

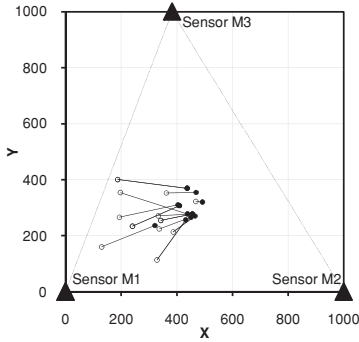


Fig. 5. Examples of actual source locations (filled circles) and their corresponding estimators (non-filled circles) joined by line segments.

**4.1.2 Source Strength Estimation.** Using the source location estimate  $(\hat{x}_u, \hat{y}_u)$ , we have three source strength estimates  $A_u$  given by  $\hat{A}_i = \bar{m}_i \hat{r}_i^2$ , for  $i = 1, 2, 3$ , where  $\hat{r}_i = \sqrt{(x_i - \hat{x}_u)^2 + (y_i - \hat{y}_u)^2}$ . We combine these three estimators using coefficients that are inversely proportional to their variance estimates. Since for the Poisson process, both the mean and variance are given by its parameter  $\bar{m}_i$ , more weight is given to estimates with a lower variance. Thus, we have the following fused source strength estimator

$$\hat{A}_u = \sum_{i=1}^3 \hat{a}_i \hat{A}_i$$

where  $\hat{a}_i = \frac{1/\bar{m}_i}{\sum_{k=1}^3 1/\bar{m}_k}$ .

Using an identical simulation configuration as the previous section, we simulated 1000 radiation sources randomly placed in the surveillance area with  $A_u = 5 \times 10^6$  CPM and  $B = 10$  CPM. The simulation result shown in Figure 7 indicate significant variations in estimated source strength. The average values of the fused source term estimator for source strengths in the range of  $[5 \times 10^5, 10^6]$  CPM are shown in Figure 8.

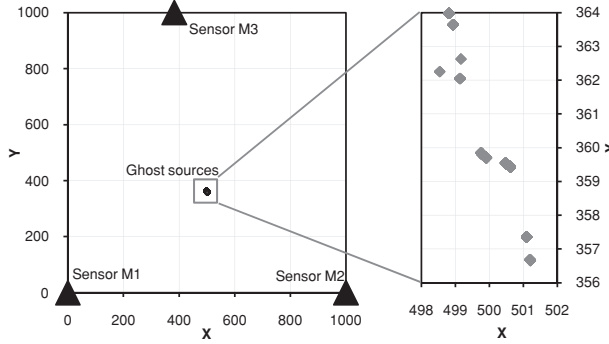


Fig. 6. Source parameter estimation algorithm produces estimates near the centroid of the triangle formed by the sensors when there is no radiation source. Expanded view of the area is on the right.

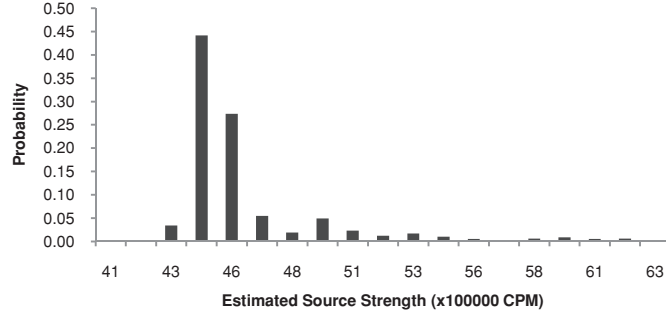


Fig. 7. Histogram of source strength estimators for  $A_u = 5 \times 10^6$  CPM,  $B = 10$  CPM showing variations of the estimates.

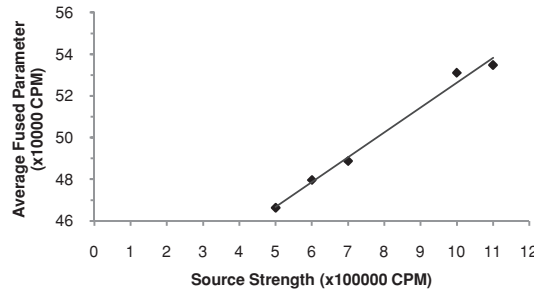


Fig. 8. Average fused source strength estimate versus actual source strength  $A_u = [5 \times 10^5, 10^6]$ .

#### 4.2 The $N$ -Sensor Case

The parameter estimation problem can also be solved using the iterative pruning (ITP) algorithm [Chin et al. 2008] when  $N > 3$  sensors are available. The advantage of having more sensors in the same area is that the robustness of the estimation increases in the face of noise and errors in the measurement

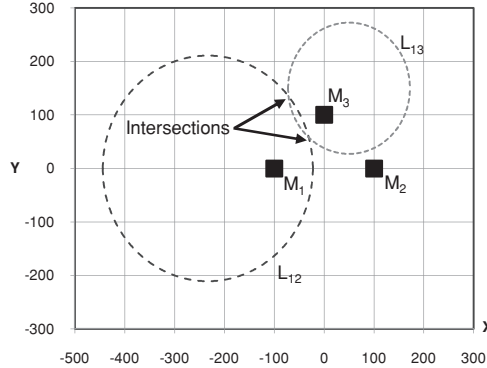


Fig. 9. Illustration of loci  $L_{12}$  and  $L_{13}$  computed by RoSD algorithm. The intersection points represent the position estimates computed.  $M_1 = (-100, 0)$ ,  $M_2 = (100, 0)$ ,  $M_3 = (0, 100)$ ,  $I_2/I_1 = 0.40$ , and  $I_3/I_1 = 3.00$ .

process. The ITP algorithm executes in two phases. In the first phase, the algorithm computes the position estimates using all combinations of 3 sensors out of  $N$  sensors. For each combination, a ratio of squared distance (RoSD) method is used to compute the position estimates. The RoSD method uses the ratio of measured source intensities, which are proportional to the inverse squared distances between the source and the sensors, to estimate the location of the source. Given the measured intensities at three locations,  $I_i = A_u/r_i^2$  for  $i = 1, 2, 3$ , RoSD computes two loci  $L_{12}$  and  $L_{13}$  that satisfy the ratio of intensity measurements where

$$L_{ij} = \{(x, y) | m_j/m_i = [(x_i - x_u)^2 + (y_i - y_u)^2]/[(x_j - x_u)^2 + (y_j - y_u)^2]\}.$$

An example of the loci and their intersections is shown in Figure 9.

The RoSD method computes the source position estimates by solving the equation  $L_{12} = L_{13}$ . The solutions of the equation are given by

$$\hat{A}_u = [L_{12}^x \ L_{12}^y]^\top + L_{12}[\cos(\beta \pm \theta) \ \sin(\beta \pm \theta)]^\top, \quad (1)$$

where

$$\beta = \arctan \frac{L_{13}^y - L_{12}^y}{L_{13}^x - L_{12}^x} \quad \theta = \arccos \frac{L_{12}^r{}^2 - L_{13}^r{}^2 + C}{2L_{12}^r\sqrt{C}} \quad C = (L_{13}^x - L_{12}^x)^2 + (L_{13}^y - L_{12}^y)^2$$

$$L_{ij}^x = \frac{m_i x_i - m_j x_j}{m_i - m_j} \quad L_{ij}^y = \frac{m_i y_i - m_j y_j}{m_i - m_j} \quad L_{ij}^r = \frac{\sqrt{(x_i - x_j)^2 + (y_i - y_j)^2}}{m_i - m_j} \sqrt{m_i m_j}.$$

In general, there are two solutions to the equation  $L_{12} = L_{13}$ . The ambiguity is resolved in the second phase of the algorithm. In the second phase, the algorithm finds the smallest region in which there are at least half of all  $2 \times \binom{N}{3}$  position estimates, called the *candidate estimates*. Starting with all the candidate estimates, the algorithm iteratively prunes at least half of the search space that contains a smaller number of the candidate estimates, until the remaining space is smaller than a threshold. Then, the weighted centroid of

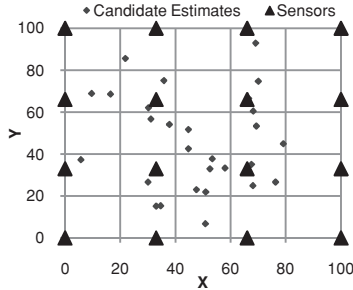


Fig. 10. Example of ghost sources computed by ITP when no radiation source is present. The triangles denote the locations of the sensors, and the diamonds denote the locations of the ghost sources.

the remaining candidate estimates is computed as the final position estimate of the radioactive source.

The overall complexity of ITP algorithm is  $O(N^3 \lg A)$ , where  $A$  denotes the area of the surveillance region [Chin et al. 2008]. In the first phase, the complexity of choosing 3 out of  $N$  sensors is  $O(N^3)$ , and computing the position estimate for each combination is  $O(1)$ . In the second phase, the complexity of pruning the search space is  $O(N^3 \lg A)$ , where  $A$  denotes the area of the surveillance region.

Although localization using  $N$  sensors is more robust, the ghost source problem discussed in Section 4.1.1 applies to ITP localization as well. That is, if we run ITP localization even if there is no radioactive source present, the algorithm may still return a position and strength estimate. For instance, Figure 10 shows a scenario in which there are 20 sensors but no radioactive source. ITP still estimates a “position” for the ghost source. We need to devise an identification method to reject such ghost sources.

## 5. SOURCE DETECTION

In this section, we describe an SPRT for detecting the presence of a source of estimated rate  $\hat{A}_u$  against the estimated background rate of  $\hat{B}_i$ . The SPRT is to be executed at a centralized server because it requires the source parameters estimated previously at the server (see Section 4).

### 5.1 SPRT Test

Consider the measurements  $m_{i,1}, m_{i,2}, \dots, m_{i,n_i}$  collected by sensor  $M_i$  within a given time window and the estimate of background radiation  $\hat{B}_i$  at this sensor location. By the definition of the Poisson process with parameter  $C$ , we have

$$P(m_{i,j}) = \frac{C^{m_{i,j}} e^{-C}}{m_{i,j}!}.$$

We utilize the estimate  $C = \hat{A}_u/\hat{r}_i^2 + \hat{B}_i$  if the source is present, and  $C = \hat{B}_i$  if the source is not present. Let  $H_C$ , for  $C \in \{\hat{A}_u/\hat{r}_i^2 + \hat{B}_i, \hat{B}_i\}$ , denote the hypothesis that the measurements correspond to the intensity level  $C$  at the sensor  $M_i$ .

Now consider the likelihood function

$$L_{\hat{A}_u/r_i^2, \hat{B}_i; n_i} = \frac{l(m_{i,1}, m_{i,2}, \dots, m_{i,n_i} | H_{\hat{A}_u/r_i^2 + \hat{B}_i})}{l(m_{i,1}, m_{i,2}, \dots, m_{i,n_i} | H_{\hat{B}_i})},$$

where

$$l(m_{i,1}, m_{i,2}, \dots, m_{i,n_i} | H_C) = \prod_{j=1}^{n_i} \frac{C^{m_{i,j}} e^{-C}}{m_{i,j}!}.$$

In the preceding, we utilize the statistical independence property of the measurements. Let the detection error probabilities be  $P(\text{accept } H_{\hat{A}_u/r_i^2 + \hat{B}_i} | H_{\hat{B}_i}) = P_{1,0}$  (i.e., false alarm rate) and  $P(\text{accept } H_{\hat{B}_i} | H_{\hat{A}_u/r_i^2 + \hat{B}_i}) = P_{0,1}$  (i.e., missed detection rate). It is shown that [Johnson 1961]

$$E(L_{\hat{A}_u/r_i^2, \hat{B}_i; n_i} | H_{\hat{B}_i} \text{ is true and } H_{\hat{A}_u/r_i^2 + \hat{B}_i} \text{ accepted}) = \frac{1 - P_{0,1}}{P_{1,0}} \quad (2)$$

and

$$E(L_{\hat{A}_u/r_i^2, \hat{B}_i; n_i}^{-1} | H_{\hat{A}_u/r_i^2 + \hat{B}_i} \text{ is true and } H_{\hat{B}_i} \text{ accepted}) = \frac{P_{0,1}}{1 - P_{1,0}}. \quad (3)$$

Equation (2) states that the expected value of the likelihood ratio is  $\frac{1 - P_{0,1}}{P_{1,0}}$  when we have a false alarm. In other words, if we declare a source to be present when  $L_{\hat{A}_u/r_i^2, \hat{B}_i; n_i} > \frac{1 - P_{0,1}}{P_{1,0}}$ , the false alarm rate will be less than  $P_{1,0}$ . Hence, we would obtain nearly the smallest possible number of samples if we declare a detection as soon as  $L_{\hat{A}_u/r_i^2, \hat{B}_i; n_i}$  is larger than  $\frac{1 - P_{0,1}}{P_{1,0}}$ . By a similar argument as Eq. (3), we would obtain nearly the smallest possible number of samples if we declare nondetection as soon as  $L_{\hat{A}_u/r_i^2, \hat{B}_i; n_i}$  is less than  $\frac{P_{0,1}}{1 - P_{1,0}}$ .

In summary, the SPRT procedure can be described as follows:

- (i) If  $L_{\hat{A}_u/r_i^2, \hat{B}_i; n_i} < \frac{P_{0,1}}{1 - P_{1,0}}$ , then declare the background, namely  $H_{\hat{B}_i}$ ;
- (ii) Else if  $L_{\hat{A}_u/r_i^2, \hat{B}_i; n_i} > \frac{1 - P_{0,1}}{P_{1,0}}$ , then declare that a source of intensity  $\hat{A}_u$  is present at location  $(\hat{x}_u, \hat{y}_u)$ , namely  $H_{\hat{A}_u/r_i^2 + \hat{B}_i}$ ;
- (iii) Otherwise, declare that the measurements are not sufficient to make a decision and continue collecting additional measurements.

The following are the important properties of the SPRT [Johnson 1961].

- (a) The expected false alarm and missed detection rates of SPRT are given by  $P_{1,0}$  and  $P_{0,1}$ , respectively.
- (b) SPRT also minimizes the expected number of steps needed to reach a decision in a very general sense. More precisely, among all tests to decide between  $H_{\hat{A}_u/r_i^2 + \hat{B}_i}$  and  $H_{\hat{B}_i}$  with the given  $P_{1,0}$  and  $P_{0,1}$ , SPRT minimizes  $E[n_i | H_{\hat{B}_i}]$  and  $E[n_i | H_{\hat{A}_u/r_i^2 + \hat{B}_i}]$  (see Wetherill [1966, Thm, 2.4], for example).

This test can be compactly expressed as

$$\frac{P_{0,1}}{1 - P_{1,0}} \leq L_{\hat{A}_u/r_i^2, \hat{B}_i; n_i} \leq \frac{1 - P_{0,1}}{P_{1,0}},$$

which can also be expressed in terms of the sum of measurements:

$$\frac{\ln\left[\frac{P_{0,1}}{1-P_{1,0}}\right] + n_i \hat{A}_u / \hat{r}_i^2}{\ln\left[\frac{\hat{A}_u / \hat{r}_i^2 + \hat{B}_i}{\hat{B}_i}\right]} \leq \sum_{j=1}^{n_i} m_{i,j} \leq \frac{\ln\left[\frac{1-P_{0,1}}{P_{1,0}}\right] + n_i \hat{A}_u / \hat{r}_i^2}{\ln\left[\frac{\hat{A}_u / \hat{r}_i^2 + \hat{B}_i}{\hat{B}_i}\right]} \quad (4)$$

Notice that the bounds on the measurement sum  $\sum_{j=1}^n m_{i,j}$  increase linearly with the number of measurements.

The above SPRT is derived under the assumption that the measurements corresponding to both background and source radiation satisfy the Poisson distribution. While point radioactive sources follow such a distribution, it may not be the case for background radiation of a more complex nature, primarily because the background radiation could be a combination of multiple sources. In such a case, the false alarm rate of our SPRT method can be different, and can be approximated by the area under the background rate distribution  $P_B(x)$  for  $x \leq \ln\left(\frac{1-P_{0,1}}{P_{1,0}}\right) + n_i \frac{\hat{A}_u / \hat{r}_i^2}{\ln((\hat{A}_u / \hat{r}_i^2 + \hat{B}_i) / \hat{B}_i)}$ . This distribution can be estimated by utilizing the empirical distribution of the background radiation at the sensor locations.

## 5.2 Expected Detection Time

In this section, we show that using an accurate estimate of the source strength will minimize the expected detection time. We proceed by dividing all sides of Eq. (4) by  $n_i$ , yielding

$$\bar{m}_i = \frac{\sum_{j=1}^n m_{i,j}}{n_i} \leq \frac{\ln\left(\frac{1-P_{0,1}}{P_{1,0}}\right) + n_i \cdot \hat{A}_u / \hat{r}_i^2}{n_i \ln\left(\frac{\hat{A}_u / \hat{r}_i^2 + \hat{B}_i}{\hat{B}_i}\right)} \quad (5)$$

for the upper threshold, and

$$\bar{m}_i = \frac{\sum_{j=1}^n m_{i,j}}{n_i} \geq \frac{\ln\left(\frac{P_{0,1}}{1-P_{1,0}}\right) + n_i \cdot \hat{A}_u / \hat{r}_i^2}{n_i \ln\left(\frac{\hat{A}_u / \hat{r}_i^2 + \hat{B}_i}{\hat{B}_i}\right)} \quad (6)$$

for the lower threshold. As the following derivation will be the same for both Eqs. (5) and (6), we express both equations as

$$\bar{m}_i = \frac{\sum_{j=1}^n m_{i,j}}{n_i} \leq \frac{\ln P + n_i \cdot \hat{A}_u / \hat{r}_i^2}{n_i \ln\left(\frac{\hat{A}_u / \hat{r}_i^2 + \hat{B}_i}{\hat{B}_i}\right)} \quad (7)$$

for  $P = \{\frac{P_{0,1}}{1-P_{1,0}}, \frac{1-P_{0,1}}{P_{1,0}}\}$ . Solving the above equation for the critical value of  $n_i$  such that the above inequality holds, we have

$$n_i = \frac{\ln P}{\bar{m}_i \ln\left(\frac{\hat{A}_u / \hat{r}_i^2 + \hat{B}_i}{\hat{B}_i}\right) - \hat{A}_u / \hat{r}_i^2} \quad (8)$$

The number of measurements required for SPRT to conclude  $H_{\hat{A}_u / \hat{r}_i^2 + B}$  (or  $H_B$  respectively) is given by Eq. (8) if  $n_i$  evaluates to a positive value. A nonpositive value of  $n_i$  denotes that SPRT will never conclude  $H_{\hat{A}_u / \hat{r}_i^2 + B}$  (or  $H_B$  respectively).

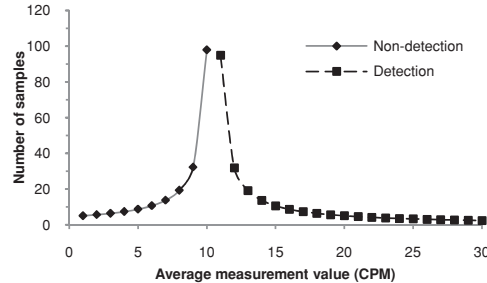


Fig. 11. Number of samples for SPRT to make a conclusion with varying average sensor measurement for  $A_u/r_i^2 = 1$  CPM,  $B_i = 10$  CPM,  $P_{0,1} = 0.01$ ,  $P_{1,0} = 0.01$ .

Differentiating Eq. (8) with respect to  $\hat{A}_u$  yields

$$\frac{\partial n_i}{\partial \hat{A}_u} = \frac{\ln P \left( 1 - \frac{\bar{m}_i}{\hat{A}_u/r_i^2 + \hat{B}_i} \right)}{\hat{r}_i^2 \left( \bar{m}_i \ln \frac{\hat{A}_u/r_i^2 + \hat{B}_i}{\hat{B}_i} - \hat{A}_u/\hat{r}_i \right)^2}. \quad (9)$$

By solving  $\frac{\partial n_i}{\partial \hat{A}_u} = 0$ , we find the threshold  $\hat{A}_i$  that yields the minimum detection time as

$$\frac{\hat{A}_u}{\hat{r}_i^2} = \bar{m}_i - \hat{B}_i \quad (10)$$

The preceding computation concludes that the detection/non-detection time is minimum if the localization step can provide accurate strength and position estimate of the source as input to the SPRT detection. Because  $\hat{B}_i$  and  $\hat{A}_u/\hat{r}_i^2$  are estimated, errors in the estimation may cause an undesirably long detection time. Furthermore, variance of  $\bar{m}_i$  is relatively large because it is averaged over a small number of samples. We quantify the number of measurements required in the presence of imperfect estimations and measurements. Figure 11 shows the number of measurements required for SPRT to conclude either  $H_{\hat{A}_u/r_i^2 + \hat{B}_i}$  or  $H_{\hat{B}_i}$  for a source measurement that is only 10% higher than the background, and false alarm and missed detection rates both equal to 1%. The figure shows that even with a low dose radioactive source, SPRT can make a conclusion using 97 samples on average. This corresponds to 6 minutes of measurements using an RFTrax radiation sensor with a 4 second sampling interval.

We use simulations to substantiate the above conclusion. We simulate a radiation sensor collecting measurements at regular intervals. First, the radiation sensor is subjected to background radiation only for 1500 measurement samples collected. The background radiation is modeled as a Poisson random variable with mean  $\lambda_B = 10$  CPM. Subsequently, a radiation source is introduced and the measurements are modeled as a Poisson random variable with mean  $\lambda_{A_u/r_i^2 + B} = \lambda_B + A_u/r_i^2$ , where  $A_u/r_i^2$  denotes the strength observed by the sensor due to the radiation source. We perform SPRT on the measurements collected. In the first attempt, we use a fixed constant multiple of the background estimate as the source strength estimate  $\hat{A}_u/\hat{r}_i^2 = f\hat{B}_i$ . We explore values of

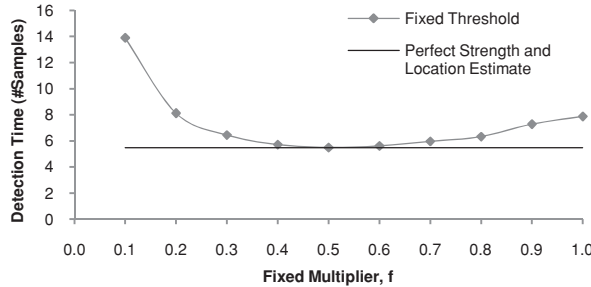


Fig. 12. Detection time of different values of  $f$ .  $A_u/r_i^2 = 5$ ,  $P_{0,1} = P_{1,0} = 0.01$ .

$f$  between 0.1 and 1.0. In the second attempt, we assume perfect estimate of the source strength and distance, that is,  $\hat{A}_u/\hat{r}_i^2 = A_u/r_i^2$ . Figure 12 shows the detection time using perfect estimates of the strength and location vs. using a fixed threshold for detection. The figure shows that perfect strength and location estimates always yield the minimum detection time. This result indicates that if the strength and the location of the radiation source are not known in advance, the proposed identification method will outperform a fixed threshold detection method.

Despite a shorter detection time, the proposed identification method has a slightly higher false alarm rate than the fixed threshold detection method, but the increment does not exceed the specified expected false alarm rate  $P_{1,0}$ . Table I shows the achieved average false alarm rate of the fixed threshold method (the T column), and the proposed identification method (the P column). The false alarm of the proposed identification method decreases as the source intensity increases. The fixed threshold detection method, however, exhibits relatively stable false alarm rate. Table II shows the achieved average missed detection rate. The result suggests that obtaining accurate estimate of the strength and location of the radiation source is desirable as it reduces the missed detection rate. As shown in the table, when  $A_u/r_i^2 < f\hat{B}_i$ , the missed detection rate increases beyond the predefined threshold  $P_{0,1}$ . This is because the fixed threshold method expects the source strength to be higher than the threshold  $f\hat{B}_i$ . As the actual source strength is lower than the predefined threshold in this case, the method incorrectly concludes that no source is present, which leads to a high missed detection rate.

## 6. IDENTIFICATION METHOD

We now combine the source parameter estimation and SPRT methods in the previous sections to develop a method for source identification. The identification method will be executed at a centralized server. Initially, the system is put into training mode where the background radiation measurements are collected by each sensor and averaged to estimate the local background radiation level  $\hat{B}_i$ . Then, the network is put into monitoring mode, and the identification of the source is achieved using the following procedure.

Table I. Achieved False Alarm Rates by the Fixed Threshold Detection Method (the T column) and the Proposed Identification Method (the P column). The Fixed Threshold is Set to  $f = 0.3$ .  $P_{0,1} = 0.1$

$P_{1,0}$	Achieved Average False Alarm Rate							
	$A_u/r_i^2 = 1$		$A_u/r_i^2 = 3$		$A_u/r_i^2 = 5$		$A_u/r_i^2 = 10$	
	T	P	T	P	T	P	T	P
0.01	0.0055	0.0078	0.0055	0.0055	0.0055	0.0041	0.0055	0.0025
0.05	0.0291	0.0396	0.0293	0.0293	0.0291	0.0217	0.0289	0.0096
0.10	0.0593	0.0817	0.0594	0.0594	0.0593	0.0427	0.0589	0.0179
0.15	0.0868	0.1229	0.0869	0.0869	0.0868	0.0635	0.0865	0.0204
0.20	0.1161	0.1645	0.1162	0.1162	0.1161	0.0764	0.1156	0.0320
0.25	0.1455	0.2086	0.1458	0.1458	0.1457	0.1042	0.1452	0.0347

Table II. Achieved Missed Detection Rates by the Fixed Threshold Detection Method (the T column) and the Proposed Identification Method (the P column). The Fixed Threshold is Set to  $f = 0.3$ .  $P_{1,0} = 0.1$

$P_{0,1}$	Achieved Average Missed Detection Rate							
	$A_u/r_i^2 = 1$		$A_u/r_i^2 = 3$		$A_u/r_i^2 = 5$		$A_u/r_i^2 = 10$	
	T	P	T	P	T	P	T	P
0.01	0.6328	0.0124	0.0069	0.0069	0.0001	0.0050	0.0000	0.0026
0.05	0.6726	0.0473	0.0335	0.0335	0.0008	0.0251	0.0000	0.0151
0.10	0.6961	0.0905	0.0647	0.0647	0.0031	0.0490	0.0000	0.0273
0.15	0.7145	0.1334	0.0991	0.0991	0.0081	0.0722	0.0000	0.0302
0.20	0.7283	0.1765	0.1339	0.1339	0.0149	0.0935	0.0001	0.0464
0.25	0.7342	0.2170	0.1580	0.1580	0.0210	0.1293	0.0003	0.0501

- (i) Using the readings from the sensors, we estimate the source location  $(\hat{x}_u, \hat{y}_u)$  and compute the source intensity estimate  $\hat{A}_u$ .
- (ii) Using the source location estimate obtained in the previous step, the thresholds of  $H_{\hat{A}_u/r_i^2 + \hat{B}_i}$  or  $H_{\hat{B}_i}$  are determined. We utilize SPRT  $L_{\hat{A}_u/r_i^2, \hat{B}_i; n_i}$  to conclude  $H_{\hat{A}_u/r_i^2 + \hat{B}_i}$  versus  $H_{\hat{B}_i}$  at sensor  $M_i$ . We declare  $H_{\hat{A}_u/r_i^2 + \hat{B}_i}$  or  $H_{\hat{B}_i}$  if and only if the respective threshold conditions, namely  $L_{\hat{A}_u/r_i^2, \hat{B}_i; n_i} > \frac{1-P_{0,1}}{P_{1,0}}$  or  $L_{\hat{A}_u/r_i^2, \hat{B}_i; n_i} < \frac{P_{0,1}}{1-P_{1,0}}$ , are satisfied at a majority of the sensors  $M_i$ ,  $i = 1, 2, 3$ . Otherwise, more measurements will be collected.

Initially, the default hypothesis is  $H_{\hat{B}_i}$ , and the hypothesis will be changed only if  $H_{\hat{A}_u/r_i^2 + \hat{B}_i}$  is declared by a majority of sensors. The above procedure has the minimum false alarm rate of the majority sensors that declare  $H_{\hat{A}_u/r_i^2 + \hat{B}_i}$  to assert the presence of a source. Figure 13 shows a functional diagram illustrating the identification method.

### 6.1 Evaluation of Identification Method with 3 Sensors

We evaluate the above identification method by simulations. We measure the effectiveness of the algorithm by evaluating the detection rate, false alarm rate, and detection time by varying  $P_{0,1}$ ,  $P_{1,0}$  and  $A_u$ . In the simulations, we randomly generate 1000 radiation sources of strengths  $A_u = 10^5, 5 \times 10^5, 6 \times 10^5, 7 \times 10^5, 10 \times 10^5$  CPM. The average increase in the radiation level over the background at these source strengths is below 10% for most of the cases,

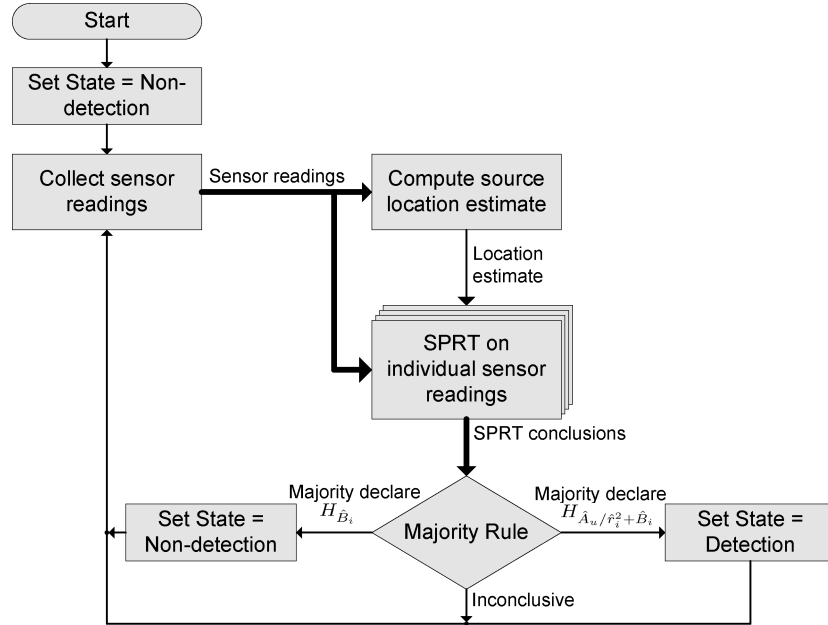


Fig. 13. Functional diagram illustrating the proposed identification method. Thick and thin arrows denote vector and scalar data, respectively.

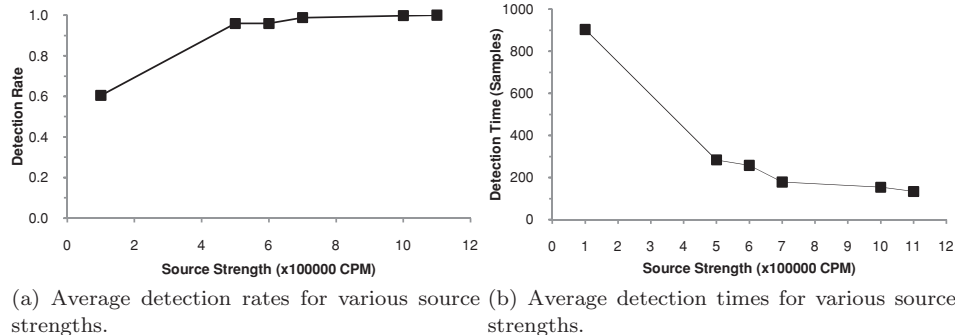
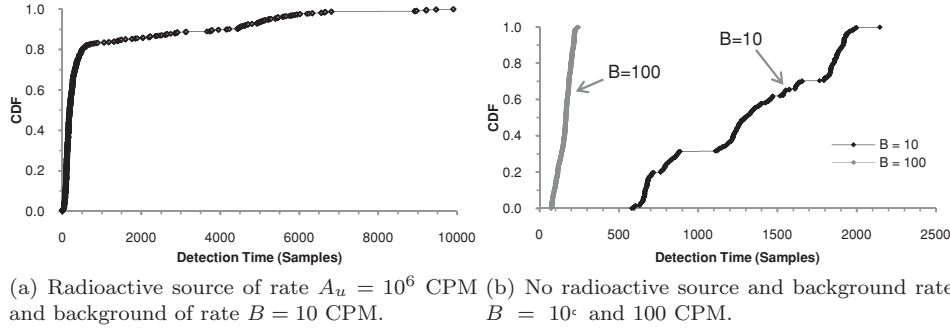


Fig. 14. Performance of the proposed identification method.

as shown in Figure 4. However, over a short time period, variations due to the background could reach 100%. The detection rates for various source strengths are shown in Figure 14(a) for  $P_{0,1} = P_{1,0} = 0.1$ , which is 100% for  $A_u = 10^6$  CPM or higher. Note that the detection rate is higher than 95% for  $A_u = 5 \times 10^5$  CPM or higher even though the average increase in the radiation level at the sensor locations is within the range of [5, 10] percent.

The detection times are shown in Figure 14(b), which show a decreasing trend with increasing  $A_u$ . The trend is expected as it is easier to detect sources of higher strengths. The average detection time is less than 300 samples (or



(a) Radioactive source of rate  $A_u = 10^6$  CPM (b) No radioactive source and background rate and background of rate  $B = 10$  CPM.  $B = 10^c$  and 100 CPM.

Fig. 15. Cumulative probability distribution of detection times for the source and background radiation.

measurements) for  $A_u = 5 \times 10^5$  CPM or higher, even though the average increase in the radiation level at the sensor locations is within [5, 10] percent. However, the actual detection times show significant variations as shown in Figure 15(a), for the case of  $A_u = 10^6$  CPM.

When no source is present, the ghost source will be likely located at the centroid of the triangle formed by the sensors. In this case, however, the corresponding high threshold for  $H_{\hat{A}_u/r_i^2+B_i}$  in Step (ii) will not be met and hence, the false alarm will be cleared. In our simulations with 10000 measurements with  $B = 10$  and 100 CPM, the proposed method does not generate any false alarm. However, the average detection times are 159 and 1309 samples for  $B = 10$  and  $B = 100$  CPM, respectively. Nonetheless, the actual detection times have a high variation as shown in Figure 15(b).

When the expected background radiation level varies among sensors, we expect the detection time to increase because the location and strength estimates of the source become less accurate. Generally, the larger the differences in the background radiation level, the longer the detection time. We evaluate the effects of the background level by comparing the detection time and detection rate for dissimilar background levels ( $\langle B_1, B_2, B_3 \rangle = \langle 10, 20, 30 \rangle, \langle 10, 30, 50 \rangle$ ) with the case of a uniform background level ( $B_1 = B_2 = B_3 = 10$ ). The simulation results presented in Figure 16 agree with our predictions. The average (and median) detection time with uniform background radiation level is 230.96 (median = 37), whereas the average (and median) detection time with non-uniform background levels are 341.56 (median = 63) and 619.83 (median = 74) for  $\langle B_1, B_2, B_3 \rangle = \langle 10, 20, 30 \rangle$  and  $\langle 10, 30, 50 \rangle$ , respectively. In all cases, the achieved detection is 94%, which is higher than the specified 90% detection rate.

It is instructive to compare our method with existing approaches.

- (a) Compared with the existing detection methods, our method has a more focused goal of detecting the point source rather than a general increase in radiation readings. The SPRT guarantees that it is uniformly the most powerful test at a given false alarm rate, in terms of maximizing the detection rate and minimizing the detection time.

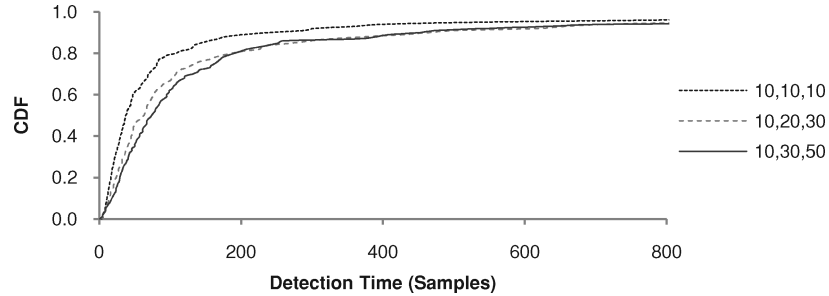


Fig. 16. Cumulative probability distribution of detection times for varying background at different sensor locations. The dotted, dash, and solid lines denote uniform background level ( $B_1 = B_2 = B_3 = 10$ ),  $(B_1, B_2, B_3) = (10, 20, 30)$ , and  $(B_1, B_2, B_3) = (10, 30, 50)$ , respectively. The sensors are located at  $S_1 = (0, 0)$ ,  $S_2 = (1000, 0)$ ,  $S_3 = (600, 1000)$ ,  $P_{0,1} = P_{1,0} = 0.1$ .

- (b) Compared with the existing estimation methods, the ghost source phenomenon is strictly controlled by the false alarm probability in our method. Furthermore, the in-situ estimation of background radiation levels makes it sensitive to variations in the background radiation across the deployment region.
- (c) Compared with existing methods that utilize a detection method followed by estimation, the proposed method achieves a lower false alarm rate since the SPRT does not have to account for all the possible source levels.

## 6.2 Evaluation of Identification Method with $N$ Sensors

We now evaluate the identification method in conjunction with the  $N$ -sensor ITP algorithm reviewed in Section 4.2. Similar to the 3-sensor case, we measure the effectiveness of the algorithm by evaluating the detection rate, false alarm rate, and detection time by varying  $P_{0,1}$ ,  $P_{1,0}$  and  $A_u$  in simulations. We use the same simulation setup as in Section 6.1, except that ITP is now used as the localization method. Note that the size of the surveillance area remains unchanged although the number of sensors has increased.

The CDF and statistics of the detection times are shown in Figure 17 and Table III, respectively, for two levels of the source strength. A system with  $N > 3$  sensors achieves faster detection compared with the case of 3 sensors. With 20 sensors, the median detection time is merely 6 samples compared with 188 samples for 3 sensors (the DTOA plot in Figure 17(b) shows the detection time in log scale). The improvement is due to the increased localization accuracy of ITP, which increases as the number of sensors increases. As discussed in Section 5.2, the detection time is at a minimum when the source strength and position estimates are exact.

The detection time of a lower-strength source is longer because such a source is harder to distinguish from background radiation. This is shown in Figure 17, in which the median detection time is 117 samples for a source strength of  $1 \times 10^5$  CPM, compared with 5 samples for a strength of  $10 \times 10^5$  CPM. In addition, we observe that the detection time grows as the number of sensors

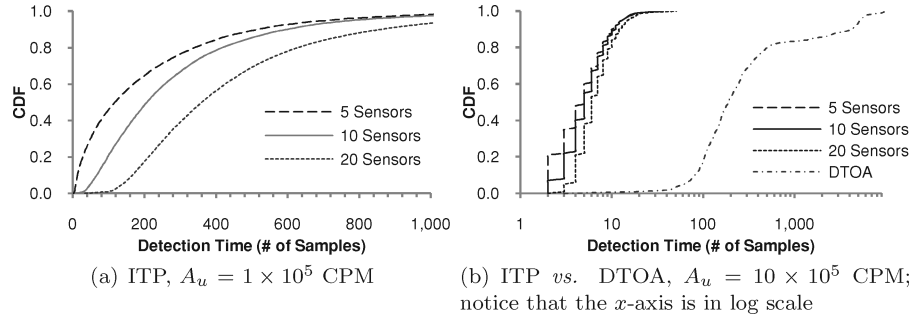


Fig. 17. Cumulative probability distribution of detection times with 5, 10, and 20 sensors. Background radiation = 10 CPM,  $P_{1,0} = P_{0,1} = 0.1$ .

Table III. Statistics of Detection Time for 20000 Repetitions with 5, 10, and 20 Sensors. Background Radiation = 10 CPM,  $P_{1,0} = P_{0,1} = 0.1$

Number of Sensors	$A_u = 1 \times 10^5$ CPM			$A_u = 10 \times 10^5$ CPM		
	5	10	20	5	10	20
Average	209.65	284.09	454.35	5.56	6.06	7.37
Median	117	207	360.5	5	5	6
StDev	263.94	256.20	328.49	3.76	3.58	3.96

increases. Comparing Figure 17(a) and Figure 17(b), we notice that the median detection time increases from 117 samples for 5 sensors, to 360.5 samples for 20 sensors. This is because increasing the number of sensors means that more sensors need to agree on the same conclusion before a decision is made. For instance, when there are 5 sensors, only 3 of them need to conclude  $H_{\hat{A}_u/r_i^2 + \hat{B}_i}$  before declaring a detection. When there are 20 sensors, 14 of them need to conclude  $H_{\hat{A}_u/r_i^2 + \hat{B}_i}$  before declaring a detection. With a low-strength radioactive source, requiring many sensors to reach the same conclusion will take longer. Furthermore, some of the sensors may be far away from the source, and their measurements will have little difference from the background radiation.

For real deployments, it is oftentimes useful to have a short detection time, so that any identified threat can be handled promptly. A shorter detection time can be achieved by relaxing the specified false alarm rate of the system, but there is a tradeoff between fast detection and reliability. Figure 18 shows that increasing the allowed false alarm rate from 2% to 10% reduces the detection time by as much as 50%. Beyond 10%, the reduction in detection time becomes smaller as the allowed false alarm rate further increases. On the other hand, varying the specified missed detection rate does not reduce the detection time significantly, as shown in Figure 19. The false alarm rate, but not the missed detection rate, determines the detection time because each additional sample generally increases the likelihood that a source is present (since the source is actually present). The algorithm's output remains inconclusive before the certainty about the source has reached the specified level, which is the false alarm rate and not the missed detection rate. If the sensor measurements are

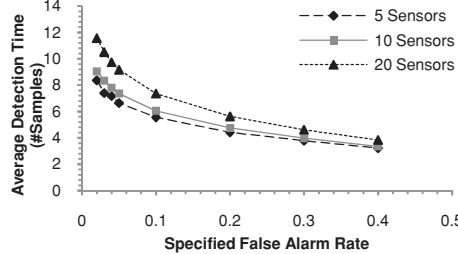


Fig. 18. Detection rate with 5, 10, and 20 sensors and varying  $P_{1,0}$ . Background radiation = 10 CPM, Source strength =  $10 \times 10^5$  CPM,  $P_{0,1} = 0.1$ .

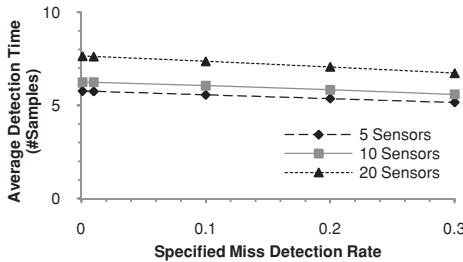


Fig. 19. Detection rate with 5, 10, and 20 sensors and varying  $P_{0,1}$ . Background radiation = 10 CPM, Source strength =  $10 \times 10^5$  CPM,  $P_{1,0} = 0.1$ .

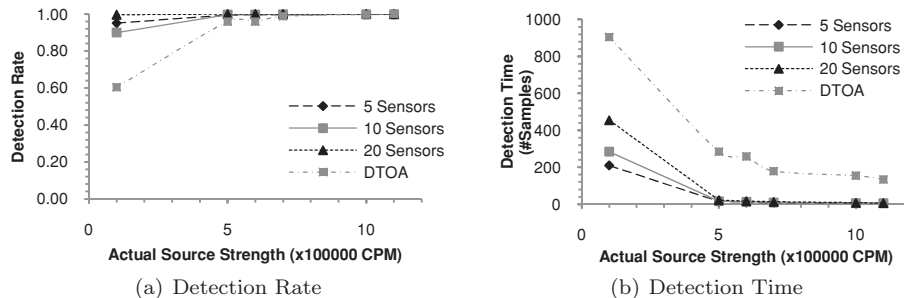


Fig. 20. Detection rate and time with 5, 10, and 20 sensors. Background radiation = 10 CPM,  $P_{1,0} = P_{0,1} = 0.1$ .

close to the background level, for example, the source is not present, then the missed detection rate plays a major role in the SPRT decision.

The detection rate metric shows the sensitivity of SPRT when dealing with low-dose radioactive sources. Figures 20(a) and 20(b) show the detection rate and the corresponding detection time for various source strengths:  $1 \times 10^5$ ,  $5 \times 10^5$ ,  $6 \times 10^5$ ,  $7 \times 10^5$ ,  $10 \times 10^5$ , and  $11 \times 10^5$  CPM. The results show that the

SPRT can effectively detect sources of very small strengths. The detection rate is close to 100% and the average detection time is less than 10 samples most of the time. The only exception is when the source strength is extremely low, at  $1 \times 10^5$  CPM, and there are only 5 or 10 sensors. In such a case, the detection rate drops to 95% (for 5 sensors) and 90% (for 10 sensors). The detection rate for 10 sensors is lower than that of 5 sensors, because in the 10 sensor case, some of the sensors are too far away for reliable measurements of the low-strength source. Because of this, it is harder for the algorithm to get a majority vote of the sensors to conclude a detection, thus lowering the detection rate. Even so, the missed detection rate does not drop below the specified missed detection rate of 10%. The result illustrates the ability of SPRT to guarantee the detection rate. The price of providing the guarantee is in the longer decision time when the measurements are less clear, that is, when the source is of a lower strength. This phenomenon is illustrated in Figure 20(b), where the detection time for a  $1 \times 10^5$  CPM source is much longer than for the higher source strengths. Comparing Figure 20(a) and 20(b), notice that even a 20-sensor network gives a high detection rate (close to 100%) when given a low-dose radioactive source, but the detection time is longer.

Compared with identification using three sensors (the DTOA plot in Figure 20), identification using  $N$  sensors improves the detection rate significantly, especially for low-strength radioactive sources. In addition, the detection time improves dramatically. For example, with a  $1 \times 10^5$  CPM source, the detection time decreases from 904 samples for 3 sensors to 210 samples for five sensors. For a high source strength such as  $10 \times 10^5$  CPM, the detection time decreases from 154 samples to only 6 samples.

A false alarm happens when SPRT concludes a detection when there is in fact no radioactive source present. The situation happens because the radiation measurements are highly variable even when there is only the background radiation present. To evaluate the false alarm rate of SPRT, we simulate scenarios in which there is no radioactive source present and  $P_{1,0}$  and  $P_{0,1}$  are varied from 5% to 30%. Our results in Figure 21 show that the actual false alarm rates achieved are well below the specified threshold. With 5 sensors in the surveillance area, the false alarm rate is only 0.33% for  $P_{0,1} = P_{1,0} = 10\%$ . With 10 and 20 sensors, there are no false alarms at all. The results show that SPRT is effective in rejecting ghost sources, while also effective in identifying the real sources. Moreover, SPRT is able to exploit information by more sensors to arrive at more accurate answers.

Unlike identification with three sensors, a varying background radiation level has minimal impact on the method with  $N$ -sensors. We simulate three scenarios with 5, 10, and 20 sensors, and three variations of the background radiation level. The first variation has all background level fixed at 10 CPM. The second variation has the background level randomly generated from a normal distribution with  $\mu = 20$  and  $\sigma = 10$ , and the third variation has  $\mu = 30$  and  $\sigma = 20$ . The exact values used are listed in Table IV. The false alarm rate, missed detection rate, and source strength used in the simulations are  $P_{0,1} = P_{1,0} = 0.1$  and  $A_u = 5 \times 10^5$  CPM, respectively. Our simulation results in Figure 22 show

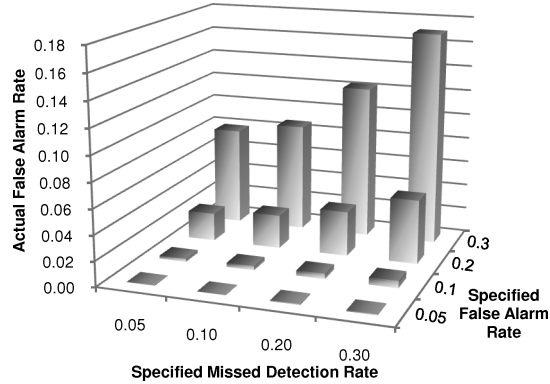


Fig. 21. False alarm rate of the identification with 5 sensors using ITP localization algorithm. Background radiation = 10 CPM.

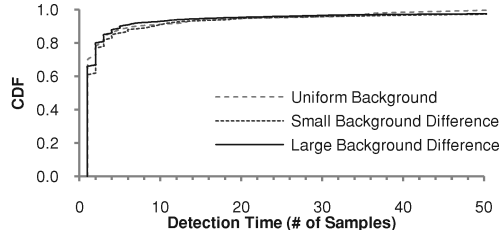
Table IV. Background Radiation Level at Each Sensor

$i$	$B_i$ (CPM)			$i$	$B_i$ (CPM)		
	Uniform	Small var.	Large var.		Uniform	Small var.	Large var.
1	10	14	40	11	10	39	15
2	10	19	8	12	10	15	49
3	10	18	37	13	10	16	40
4	10	18	19	14	10	22	40
5	10	26	23	15	10	10	52
6	10	22	63	16	10	33	10
7	10	36	47	17	10	24	56
8	10	13	51	18	10	28	29
9	10	28	3	19	10	38	21
10	10	19	24	20	10	24	30

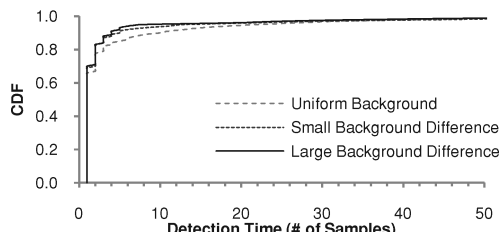
that the detection time does not change significantly even when the background radiation varies a lot. This is because the larger background radiation actually reduces the detection time slightly at some sensors due to larger variance in the readings. Although this may increase the false alarms at individual sensors, these false alarms do not impact the overall performance of the system with an increased number of sensors participating in the SPRT. The detection rate of the system remains close to 100% even at a high level of background radiation. This finding agrees with the result presented in Figure 20.

## 7. EXPERIMENTAL TEST-BED RESULTS

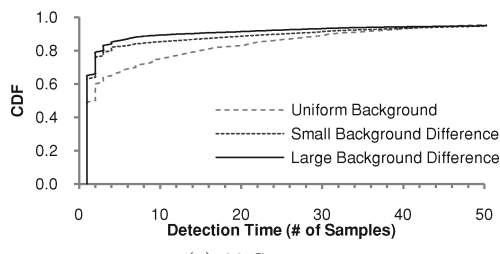
In this section, we present our test-bed experiments. First, we describe the configuration of our testbed in Section 7.1. Then, we present the sensor hardware and software in Section 7.2. We describe how we use the testbed to emulate stronger radiation sources and larger deployments in Section 7.3. In Section 7.4, we present the background radiation data collected for sensor calibration.



(a) 5 Sensors



(b) 10 Sensors



(c) 20 Sensors

Fig. 22. Cumulative probability distribution of detection times for varying background at different sensor locations.  $P_{1,0} = P_{0,1} = 0.1$ ,  $A_u = 5 \times 10^5$  CPM.

Subsequently, Section 7.5 and 7.6 present evaluation results of the proposed identification method.

### 7.1 Test-Bed System Setup

We have set up three radiation detection testbeds at (1) the SensorNet Laboratory at Oak Ridge National Laboratory (ORNL), (2) Purdue University, and (3) University of Illinois at Urbana-Champaign. All three testbeds have similar configurations. Figure 23 shows the equipment layout of the test-bed for the experiments and Figure 24 shows the test-bed setup at ORNL. The test-bed at ORNL is intended to emulate an outdoor environment similar to the ORNL courtyard shown in Figure 25. The components of the test-bed include a collection of Rad-CZT radiation sensors (currently 3 sensors) from RFTrax Inc. [RFTrax], a SensorNet node, and a wireless router.

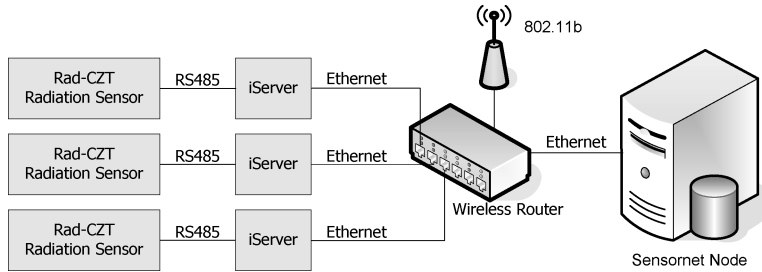


Fig. 23. Equipment setup in the radiation test-bed.

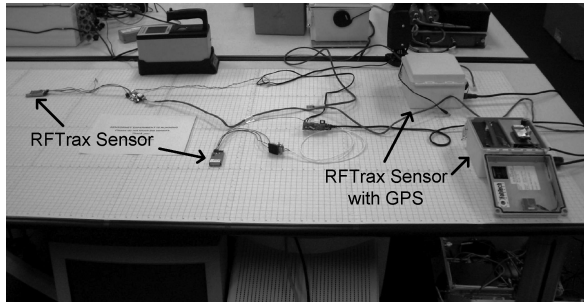


Fig. 24. Radiation detection workbench at ORNL emulating the larger courtyard shown in Figure 25.



Fig. 25. Courtyard at ORNL emulated using a small scale testbed shown in Figure 24.

For the experiments, the SensorNet node software is configured to poll each sensor every 4 seconds and store the sensor readings in a MySQL database. Because of limited storage in the SensorNet node, the database is configured to store only the 10,000 most recent samples of data. In addition to storing the sensor readings, we have augmented the SensorNet node software to send the sensor data to a workstation in real time for on-line analysis.

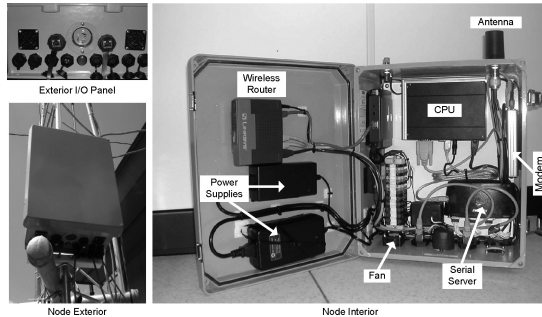


Fig. 26. The SensorNet node hardware.

## 7.2 The SensorNet Node

The SensorNet node (see Figure 26) is a rugged hardware platform developed at ORNL with the goal of allowing a wide variety of sensors to be monitored and managed over a nation-wide distributed network. The wireless router allows the SensorNet nodes to communicate with each other as well as with an Ethernet switch connecting the sensors. The radiation sensors (RS485 devices) connect to the SensorNet node via iServer [iServer]. The iServer proxies the RS485/232 interface (for the radiation sensors in this case) to an Ethernet interface, thus providing access to the sensors via TCP/IP. In some configurations, the SensorNet node may be furnished with a broadband modem for connectivity over a cellular network. This may serve as a backup link if the primary connection over Ethernet/802.11 fails.

The SensorNet node runs the standard Linux operating system (Fedora Core) and a software package (the *node software*) developed by ORNL. The node software consists of a set of daemons that, under steady-state conditions, will perform the following operations.

- Query the sensors connected to the SensorNet node for data, and populate the MySQL database with the data. In addition, the node software analyzes the data to determine if an alert event should be issued. It utilizes IEEE 1451 as a means to communicate with a wide variety of sensors/actuators. IEEE 1451 wrappers are implemented for legacy devices that do not support the standard. For modern sensors that talk IEEE 1451, plug-and-play operation can be supported.
- Listen to the control center for configuration commands, for example, setting the sensor polling rate and alert rules.
- Update the current location information for mobile SensorNet nodes and sensors.
- Archive the sensor data to a control center when requested; for example, for offline data analysis.

For communication with the control center, each SensorNet node has multiple network connections. The node software uses at least two independent

means to communicate with the control center, of which one is assigned as the primary connection. If the primary connection fails, the data are automatically rerouted through the secondary connection. The connectivity management module (CMM) monitors the health of all the network links available. The CMM periodically checks the connectivity to the control center, and reconfigures the network interface if the control center is unreachable.

### 7.3 Emulation of Larger Deployments and Stronger Sources

Our test-bed is implemented on a  $100 \times 100$  square-inch workbench shown in Figure 24 using a radioactive point source of  $0.95 \mu\text{Ci}$ . Larger monitoring areas such as the courtyard at ORNL shown in Figure 25 and stronger sources can be emulated using the testbed as follows. Let  $r_{\text{emulated}}$  and  $r_{\text{testbed}}$  be the emulated distance and actual distance on the test-bed and workbench, respectively, such that  $r_{\text{emulated}} = s_f \times r_{\text{testbed}}$ . Sensor measurements of a radioactive source of strength  $A_{\text{testbed}}/r_{\text{testbed}}^2$  in the test-bed correspond to the measurements of a source of strength  $A_{\text{emulated}} = s_f^2 A_{\text{testbed}}$  in the emulated configuration. For example,  $r_{\text{emulated}}$  is in meters for the courtyard shown in Figure 25 and  $r_{\text{testbed}}$  is in inches for the workbench. Then, we have  $s_f = 1 \text{ m}/1 \text{ inch} = 100 \text{ cm}/2.54 \text{ cm} = 39.37$ . Thus, we can emulate sources with  $A_{\text{emulated}} = 1549.99 \times A_{\text{testbed}}$  in the courtyard. The emulated source can have a strength of  $1472 \mu\text{Ci}$ , which is much higher than the safe level. Thus much stronger sources can be emulated, for the purpose of sensor measurements, in our test-bed using only much lower intensity sources, because the distances between the source and a sensor are also scaled. Hence, we are able to retain the complexity of the identification problem in the test-bed without using actual high intensity sources in the experiments. In particular, this emulation method can be used to map public open areas where radioactive sources cannot be easily deployed. However, sensors can be deployed in such areas to obtain background radiation measurements, which can then be used as measurements in the test-bed. This approach is somewhat limited when the background measurements are not the same in the emulated and workbench areas, but it would be more accurate than a simulation-only approach.

### 7.4 Background Radiation Profile

The three radiation sensors were activated to collect background radiation readings on two different days to build a background radiation profile. A total of 9,900 samples were collected at a rate of one sample every 4 seconds, for an equivalence of 11 hours' worth of data. Figure 27 reports the distribution of the background radiation. The statistics of the data collected are reported in Table V.

We performed the z-test for comparing the means of two independent samples to compare the radiation counts of the three sensors on the testbed. The test results show that the probability of two sensors producing the same mean value is 0.63% at the maximum. In other words, the mean values are different with a 99.37% level of significance, even though the sensors are located within

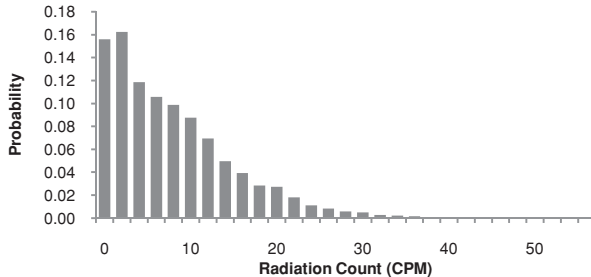


Fig. 27. Background radiation distribution in ORNL SensorNet Laboratory. Measurements were taken on July 23, 2007.

Table V. Statistics of Background Radiation in SensorNet Lab

Day 1				Day 2			
Sensor	Mean	Stdev	#Samples	Sensor	Mean	Stdev	#Samples
RFTrax1	7.80	7.12	9900	RFTrax1	7.62	7.13	9900
RFTrax2	7.46	7.01	9900	RFTrax2	7.54	7.07	9900
RFTrax3	8.08	7.46	9900	RFTrax3	8.00	7.30	9900

2 feet of each other at the maximum. This experiment concludes that each sensor requires a separate background radiation profile.

### 7.5 Localization Method

In this section, we evaluate the localization method on our testbed and report the localization errors achieved by the algorithm. On our testbed, a Cs-137 radioactive source of strength  $0.95 \mu\text{Ci}$  was used with RFTrax RAD-CZT sensors to collect measurements to estimate the locations of the source using the difference triangulation method described in Section 4.1.1. In each case, the number of measurements were within the range of [140, 170] samples. In Figure 28(a), we show example cases with different source locations and their estimates, and in Figure 28(b) we show repeated measurements with the same source and sensor locations. The performance of the localization method is summarized in Table VI, wherein the top six rows correspond to different sensor and/or source locations and the other rows correspond to repeated measurements for the same sensor and source locations. The errors in the location estimates are plotted in Figure 29 with an average error of 4.87 inches. When no source is present, the localization method returns ghost sources, as shown in the two examples in Figure 30.

### 7.6 Identification Method

In this section, we evaluate the effectiveness of the proposed identification method using our testbed. In all cases, we vary  $P_{0,1}$  and  $P_{1,0}$  to measure the detection time of the proposed method. Our results show that the identification

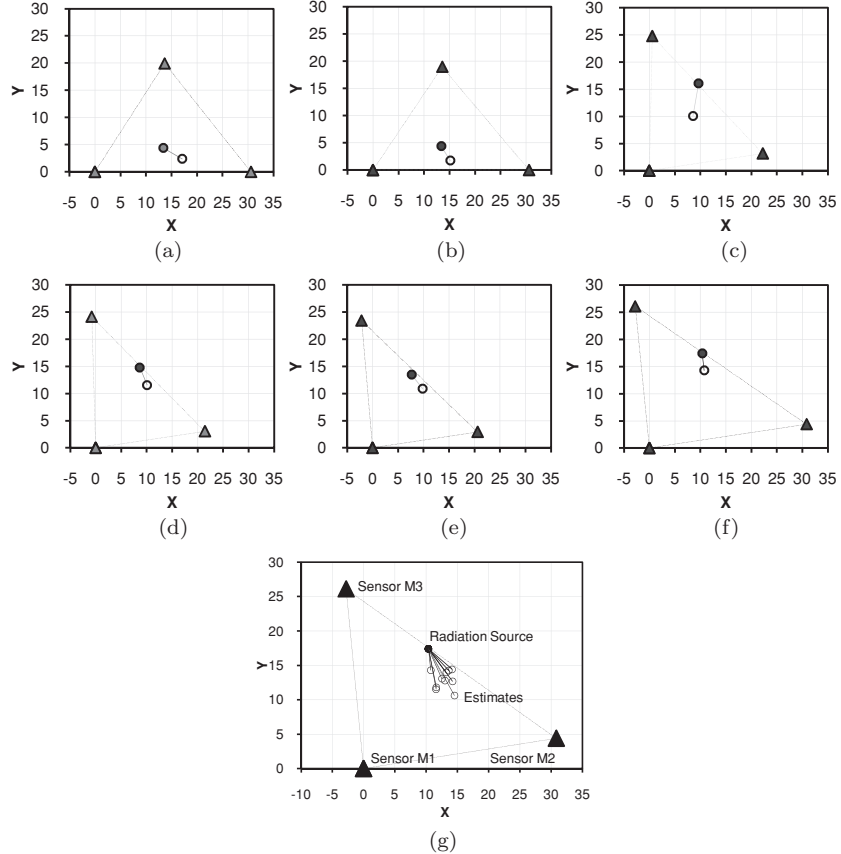


Fig. 28. Localization accuracy of a Cs-137 radioactive source with different sensors and source locations (a–f), and different measurements with the same source and sensor locations (g).

method rejected the ghost sources computed based on the background readings. However, the decision time is a function of the false alarm rate  $P_{1,0}$ . When  $P_{1,0} = 0.001$ , the detection time was 339 samples but was reduced to 28 samples when the false alarm rate was increased from 2% to 40%, as shown in Figure 31.

The source detection rate varied based on  $\tau$ , the number of initial measurements used before the SPRT was applied in the experiments. The radiation levels averaged over 10 minute intervals varied across the measurement sets both when a source was present and absent as indicated in Figure 32. For the case in Table VI with  $P_{0,1} = 0.1$ , for  $\tau \leq 10$ , the empirical false alarm rate was 0.3, and was improved to 0.1 when  $\tau = 25$ , and reached 0.0 when  $\tau = 75$ . We next examine in details the configuration that missed the detection for  $\tau = 25$ , corresponding to Row 5 in Table VI, by varying  $P_{0,1}$  in four repeated sets of measurements. The detection times are shown in Figure 31, which have lower values as we increase  $P_{0,1} = 0.001, 0.01, 0.1, 0.2, 0.3$ . Among the four sets of measurements, one set missed detecting the source for  $P_{1,0} = 0.1, 0.2, 0.3$ .

Table VI. Experiments with a Real Radioactive Source of Strength  $0.95 \mu$  Curies. The Error Column Shows the Euclidean Distance between the Actual Source Position and Estimated Source Position

Sensor $M_1$ (inches)	Sensor $M_2$ (inches)	Sensor $M_3$ (inches)	Actual Source (inches)	Estimated (inches)	Error (inches)
(0.000, 0.000)	(30.602, 0.000)	(13.675, 19.949)	(13.406, 4.386)	(17.115, 2.381)	4.217
(0.000, 0.000)	(30.602, 0.000)	(13.594, 18.953)	(13.406, 4.386)	(15.136, 1.739)	3.163
(0.000, 0.000)	(22.247, 3.171)	(0.580, 24.782)	(9.635, 16.086)	(8.544, 10.046)	6.138
(0.000, 0.000)	(21.417, 3.053)	(-0.777, 24.123)	(8.651, 14.781)	(10.082, 11.542)	3.541
(0.000, 0.000)	(20.600, 2.937)	(-2.147, 23.407)	(7.679, 13.477)	(9.818, 10.890)	3.357
(0.000, 0.000)	(30.833, 4.395)	(-2.780, 26.101)	(10.365, 17.406)	(10.743, 14.296)	3.133
(0.000, 0.000)	(30.833, 4.395)	(-2.780, 26.101)	(10.365, 17.406)	(14.519, 10.626)	7.952
(0.000, 0.000)	(30.833, 4.395)	(-2.780, 26.101)	(10.365, 17.406)	(14.225, 12.680)	6.103
(0.000, 0.000)	(30.833, 4.395)	(-2.780, 26.101)	(10.365, 17.406)	(11.588, 11.532)	6.000
(0.000, 0.000)	(30.833, 4.395)	(-2.780, 26.101)	(10.365, 17.406)	(13.602, 14.254)	4.518
(0.000, 0.000)	(30.833, 4.395)	(-2.780, 26.101)	(10.365, 17.406)	(13.223, 13.972)	4.468
(0.000, 0.000)	(30.833, 4.395)	(-2.780, 26.101)	(10.365, 17.406)	(12.517, 13.061)	4.849
(0.000, 0.000)	(30.833, 4.395)	(-2.780, 26.101)	(10.365, 17.406)	(10.743, 14.296)	3.133
(0.000, 0.000)	(30.833, 4.395)	(-2.780, 26.101)	(10.365, 17.406)	(13.007, 12.783)	5.325
(0.000, 0.000)	(30.833, 4.395)	(-2.780, 26.101)	(10.365, 17.406)	(14.143, 14.415)	4.819
(0.000, 0.000)	(30.833, 4.395)	(-2.780, 26.101)	(10.365, 17.406)	(11.626, 11.798)	5.748

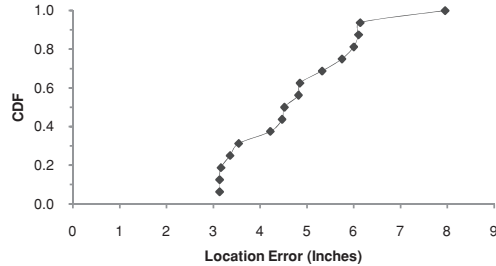


Fig. 29. Cumulative probability distribution of location estimation errors corresponding to Table VI.

## 8. CONCLUSIONS

We have addressed the identification problem of a low-level point radioactive source amidst background radiation. Our solution is achieved by a network of radiation sensors working in a tightly coupled two-step procedure. Based on measurements from the three or more sensors, the geometric difference triangulation method or the ITP algorithm is used to estimate the location and strength of the source. Then, a sequential probability ratio test based on current measurements and estimated parameters is employed to finally decide: (1) the presence of a source with the estimated parameters, or (2) the absence of the source, or (3) the insufficiency of measurements to make a decision. This method achieves the specified levels of the false alarm and missed detection probabilities, while ensuring a close-to-minimum number of measurements for reaching a decision. The proposed method minimizes the ghost-source problem of current estimation methods and achieves a lower false alarm rate compared

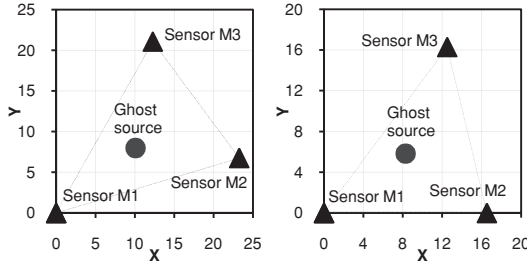


Fig. 30. Ghost sources computed and rejected in our testbed experiment.

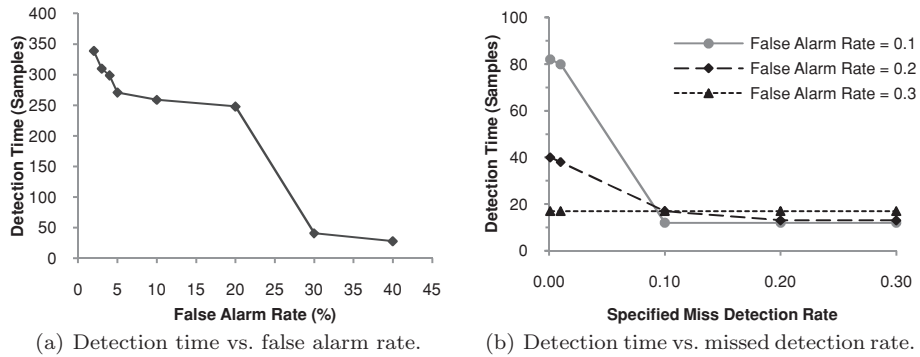


Fig. 31. Detection times of the identification method with varying false alarm and missed detection rates.

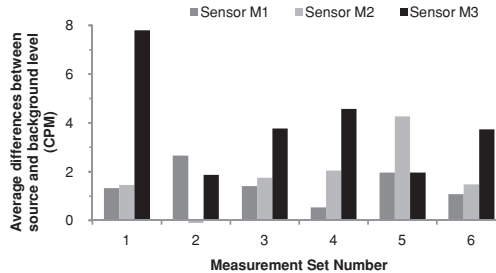


Fig. 32. Differences between average radiation levels when source is present and not present vary at each sensor across the measurement sets.

with current detection methods. We have tested and demonstrated our method using: (1) simulations, and (2) a test-bed that utilizes the scaling properties of point radioactive sources to emulate high intensity sources that cannot be easily/safely handled in practice.

Currently, the proposed identification method does not perform well when the radiation source is moving or there are multiple sources in the surveillance area. For further research, a more comprehensive identification method with low latency would be useful to identify multiple moving sources. Moreover, it

may be possible to improve the estimation of the source strength by using a training step wherein the fuser can be calibrated, for example, by determining both an offset and a scale factor.

## APPENDIX

### A. PROOF OF CORRECTNESS OF DTOA BINARY SEARCH METHOD

We prove the correctness of the binary search method by establishing that on  $L_{1,2}$  the function  $\delta_{1,3}$  varies monotonically so that the binary search can be supported.<sup>2</sup> We show the monotonicity in ln-space for the scenario where  $M_1 = (0, 0)$ ,  $M_2 = (1000, 0)$  and  $M_3 = (400, 1000)$ . The general case can be proved along the lines of Xu et al. [2010]. Without loss of generality, we assume:

- (a)  $M_1 = (0, 0)$ ,  $M_2 = (x_2, 0)$  and  $M_3 = (x_3, y_3)$  such that  $x_2 > 0$ ,  $x_3 > 0$  and  $y_3 > 0$ . Also,  $x_3 < x_2$ .
- (b) The source  $S$  is located at  $(x_u, y_u)$  such that  $x_u > 0$  and  $y_u > 0$ , and  $S$  is closer to  $M_1$  than to  $M_2$  and  $M_3$ ; otherwise, we can rotate the triangle and re-label the sensors by their coordinates.

We have  $d(S, M_i) = r_i = \sqrt{(x_u - x_i)^2 + (y_u - y_i)^2}$ , and let  $\Delta(M_i, M_j) = \ln[d(S, M_i)] - \ln[d(S, M_j)]$ , for  $i, j = 1, 2, 3$ . Then, we have

$$\frac{\partial d(S, M_i)}{\partial x_u} = \frac{(x_u - x_i)}{d(S, M_i)}$$

and

$$\frac{\partial d(S, M_i)}{\partial y_u} = \frac{(y_u - y_i)}{d(S, M_i)}.$$

By Item (b) we have  $d(S, M_1) < d(S, M_2)$  and  $d(S, M_1) < d(S, M_3)$ .

The directional derivative of  $\Delta(M_1, M_3)$  on the locus  $\{(x_u, y_u) | \Delta(M_1, M_2) = \delta_{12}\}$ , for any  $\delta_{12}$ , is given by

$$\begin{aligned} & \nabla_{\Delta(M_1, M_2)} \Delta(M_1, M_3) \\ &= \left[ \begin{array}{c} \frac{\partial \Delta(M_1, M_2)}{\partial x_u} \\ \frac{\partial \Delta(M_1, M_2)}{\partial y_u} \end{array} \right]^T \circ \frac{1}{K} \left[ \begin{array}{c} \frac{\partial \Delta(M_1, M_3)}{\partial x_u} \\ \frac{\partial \Delta(M_1, M_3)}{\partial y_u} \end{array} \right] \\ &= \left[ \begin{array}{c} \frac{x_u}{[d(S, M_1)]^2} - \frac{x_u - x_3}{[d(S, M_3)]^2} \\ \frac{y_u}{[d(S, M_1)]^2} - \frac{y_u - y_3}{[d(S, M_3)]^2} \end{array} \right]^T \circ \frac{1}{K} \left[ \begin{array}{c} \frac{x_u}{[d(S, M_1)]^2} - \frac{x_u - x_2}{[d(S, M_2)]^2} \\ \frac{y_u}{[d(S, M_1)]^2} - \frac{y_u - y_2}{[d(S, M_2)]^2} \end{array} \right] \\ &= \left( \frac{x_u}{[d(S, M_1)]^2} - \frac{x_u - x_3}{[d(S, M_3)]^2} \right) \left( \frac{x_u}{[d(S, M_1)]^2} - \frac{x_u - x_2}{[d(S, M_2)]^2} \right) \end{aligned}$$

<sup>2</sup>The monotonicity proof of Xu et al. [2010] is valid for  $\delta_{i,k} = r_i - r_k$  in the distance space as opposed to the ln-space here.

$$+ \left( \frac{y_u}{[d(S, M_1)]^2} - \frac{y_u}{[d(S, M_2)]^2} \right) \left( \frac{y_u}{[d(S, M_1)]^2} - \frac{y_u - y_3}{[d(S, M_3)]^2} \right)$$

where  $K = \left[ \left( \frac{\partial \Delta(M_1, M_3)}{\partial x_u} \right)^2 + \left( \frac{\partial \Delta(M_1, M_3)}{\partial y_u} \right)^2 \right]^{-1/2}$ .

Note that  $x_2 > 0$ ,  $x_3 > 0$  and  $y_3 > 0$ . Also  $d(S, M_3) > d(S, M_1)$  and  $d(S, M_2) > d(S, M_1)$ . Then, we conclude that  $\nabla_{\Delta(M_1, M_2)} \Delta(M_1, M_3) > 0$ , for all  $x_u > 0$  and  $y_u > 0$ .

## REFERENCES

- ANDERSON, D. N., STROMSWOLD, D. C., WUNSCHEL, S. C., PEURRUNG, A. J., AND HANSEN, R. R. 2006. Detection and location of Gamma-Ray sources with a modulating coded mask. *Technometrics* 48, 2, 252–261.
- ARCHER, D. E., BEAUCHAMP, B. R., MAUGER, G. J., NELSON, K. E., MERCER, M. B., PLETCHER, D. C., RIOT, V. J., SCHEK, J. L., AND KNAPP, D. A. 2006. Adaptable radiation monitoring system and method. U.S. Patent 7,064,336 B2.
- BAR-SHALOM, Y. AND LI, X. R. 1995. *Multitarget-Multisensor Tracking: Principles and Techniques*. YBS Publishing.
- BAR-SHALOM, Y. AND LI, X.-R. 2001. *Estimation with Applications to Tracking and Navigation*. Wiley, New York.
- BLACKMAN, S. AND POPOLI, R. 1999. *Design and Analysis of Modern Tracking Systems*. Artech House, Boston, MA.
- BRENNAN, S. M., MIELKE, A. M., AND TORNEY, D. C. 2004. Radiation detection with distributed sensor networks. *IEEE Computer*, 57–59.
- CHENG, X., THAELER, A., XUE, G., AND CHEN, D. 2004. Tps: A time-based positioning scheme for outdoor wireless sensor networks. In *Proceedings of the 23rd Annual Joint Conference of the IEEE Computer and Communications Societies (INFOCOM'04)*. IEEE Computer Society Press, Los Alamitos, CA, 2685–2696.
- CHIN, J.-C., YAU, D. K., RAO, N. S., YANG, Y., MA, C. Y., AND SHANKAR, M. 2008. Accurate localization of low-level radioactive source under noise and measurement errors. In *Proceedings of the 6th ACM Conference on Embedded Network Sensor Systems (SenSys'08)*. ACM, New York, 183–196.
- DEVROYE, L., GYORFI, L., AND LUGOSI, G. 1997. *A Probabilistic Theory of Pattern Recognition*. Springer-Verlag, Berlin.
- DING, M. AND CHENG, X. 2009. Fault-tolerant target tracking in sensor networks. In *Proceedings of MobiHoc*. ACM, New York.
- DUDA, R. O., HART, P. E., AND STORK, D. G. 2001. *Pattern Classification*. Wiley, New York.
- FEHLAU, P. E. 1993. Comparing a recursive digital filter with the moving-average and sequential probability-ratio detection methods for SNM portal monitors. *IEEE Trans. Nucl. Sci.* 40, 2, 143–146.
- GUNATILAKA, A., RISTIC, B., AND GAILIS, R. 2007. On localisation of a radiological point source. In *Proceedings of the International Conference on Information, Decision and Control*. IEEE Computer Society Press, Los Alamitos, CA.
- GUNATILAKA, A., RISTIC, B., SKVORTSOV, A., AND MORELANDE, M. 2008. Parameter estimation of a continuous chemical plume source. In *Proceedings of the International Conference on Information Fusion*. IEEE Computer Society Press, Los Alamitos, CA.
- HOWSE, J. W., TICKNOR, L. O., AND MUSKE, K. R. 2001. Least squares estimation techniques for position tracking of radioactive sources. *Automatica* 37, 1727–1737.
- iSERVER. iserver microserver products. <http://www.newportus.com/Products/ProdFam/iServer.htm>.
- JARMAN, K. D., SMITH, L. E., AND CARLSON, D. K. 2004. Sequential probability ratio test for long-term radiation monitoring. *IEEE Trans. Nuclear Sci.* 51, 4, 1662–1666.
- JOHNSON, N. L. 1961. Sequential analysis: A survey. *J. Royal Statist. Soc. Series A* 124, 3, 372–411.
- KNOLL, G. F. 2000. *Radiation Detection and Measurement*. Wiley, New York.
- KUSHNER, H. J. AND YIN, C. G. 2003. *Stochastic Approximation and Recursive Algorithms and Applications*, 2nd ed. Springer-Verlag, Berlin.

- LJUNG, L. 1998. *System Identification: Theory for the User* 2nd Ed. Prentice-Hall, Englewood Cliffs, NJ.
- MACMILLAN, N. A. AND MACMILLAN, N. A. 2004. *Detection Theory: A User's Guide* 2nd Ed. Lawrence Erlbaum Associates.
- MIELKE, A., JACKSON, D., BRENNAN, S. M., SMITH, M. C., TORNEY, D. C., MACCABE, A. B., AND KARLIN, J. 2005. Radiation detection with distributed sensor networks. In *SPIE Defense and Security Proceedings*.
- MIHALAS, D. AND MIHALAS, B. W. 2000. *Foundations of Radiation Hydrodynamics*. Courier Dover Publications.
- MORELANDE, M., RISTIC, B., AND GUNATILAKA, A. 2007. Detection and parameter estimation of multiple radioactive sources. In *Proceedings of the International Conference on Information Fusion*. IEEE Computer Society Press, Los Alamitos, CA.
- NELSON, K. E., VALENTINE, J. D., AND BEAUCHAMP, B. R. 2007. Radiation detection method and system using the sequential probability ratio test. U.S. Patent 7,244,930 B2.
- NEMZEK, R. J., DREICER, J. S., TORNEY, D. C., AND WARNOCK, T. T. 2004. Distributed sensor networks for detection of mobile radioactive sources. *IEEE Trans. Nuclear Sci.* 51, 4, 1693–1700.
- NICULESCU, D. AND NATH, B. 2003. Ad hoc positioning system (aps) using aoa. In *Proceedings of the 22nd Annual Joint Conference of the IEEE Computer and Communications Societies (INFOCOM'03)*. IEEE Computer Society Press, Los Alamitos, CA, 1734–1743.
- POOR, H. V. 1998. *An Introduction to Signal Detection and Estimation*. Springer-Verlag, Berlin.
- PRESS, W. H., TEUKOLSKY, S. A., VETTERLING, W. T., AND FLANNERY, B. P. 1992. *Numerical Recipes in C*. Cambridge University Press, Cambridge, UK.
- RAO, N. S. V., SHANKAR, M., CHIN, J.-C., YAU, D. K. Y., SRIVATHSAN, S., IYENGAR, S. S., YANG, Y., AND HOU, J. C. 2008. Identification of low-level point radiation sources using a sensor network. In *Proceedings of ACM/IEEE International Conference on Information Processing in Sensor Networks (IPSN)*. ACM, New York.
- RAO, N. S. V., XU, X., AND SAHNI, S. 2007. A computational geometric method for dtoa triangulation. In *Proceedings of the International Conference on Information Fusion*.
- RFTRAX. Rftrax rad-czt radiation sensor. <http://www.rftrax.com/radczt.html>.
- SAVVIDES, A., HAN, C.-C., AND STRIVASTAVA, M. B. 2001. Dynamic fine-grained localization in ad-hoc networks of sensors. In *Proceedings of the 7th Annual International Conference on Mobile Computing and Networking (MobiCom'01)*. ACM, New York, 166–179.
- STEPHENS, D. L. AND PEURUNG, A. J. 2004. Detection of moving radioactive sources using sensor networks. *IEEE Trans. Nuc. Sci.* 51, 5, 2273–2278.
- SUNDARESAN, A., VARSHNEY, P. K., AND RAO, N. S. V. 2007. Distributed detection of a nuclear radioactive source using fusion of correlated decisions. In *Proceedings of the International Conference on Information Fusion*.
- THAELER, A., DING, M., AND CHENG, X. 2005. itps: An improved location discovery scheme for sensor networks with long-range beacons. *J. Parall. Distrib. Comput.* 65, 98–106.
- TREES, H. L. V. 1968. *Detection, Estimation and Modulation Theory, Part I*. Wiley, New York.
- VARSHNEY, P. K. 1997. *Distributed Detection and Data Fusion*. Springer-Verlag, Berlin.
- WETHERILL, G. B. 1966. *Sequential Methods in Statistics*. Methuen and Co.
- WICKENS, T. D. 2002. *Elementary Signal Detection Theory*. Oxford University Press, Oxford, UK.
- XU, X., RAO, N. S. V., AND SAHNI, S. 2010. A computational geometry method for localization using difference of distances. *ACM Trans. Sensor. Netw.* 6, 2.  
<http://doi.acm.org/10.1145/1689239.1689240>.

Received February 2009; revised October 2009, March 2010; accepted April 2010